

2013-01-01

Dielectric And Complex Impedance Properties Of Tetravalent Hafnium (HF 4+) Integrated Cobalt Ferrite

Luis Javier Sanchez

University of Texas at El Paso, ljsanchez2@miners.utep.edu

Follow this and additional works at: https://digitalcommons.utep.edu/open_etd



Part of the [Electromagnetics and Photonics Commons](#)

Recommended Citation

Sanchez, Luis Javier, "Dielectric And Complex Impedance Properties Of Tetravalent Hafnium (HF 4+) Integrated Cobalt Ferrite" (2013). *Open Access Theses & Dissertations*. 1725.
https://digitalcommons.utep.edu/open_etd/1725

This is brought to you for free and open access by DigitalCommons@UTEP. It has been accepted for inclusion in Open Access Theses & Dissertations by an authorized administrator of DigitalCommons@UTEP. For more information, please contact lweber@utep.edu.

DIELECTRIC AND COMPLEX IMPEDANCE PROPERTIES OF
TETRAVALENT HAFNIUM (HF^{4+}) INTEGRATED
COBALT FERRITE

LUIS SANCHEZ

Department of Metallurgical and Materials Engineering

Approved:

Chintalapalle V. Ramana, Ph.D., Chair

Stephen W. Stafford, Ph.D.

David Roberson, Ph.D.

Yirong Lin, Ph.D.

Benjamin C. Flores, Ph.D.
Dean of the Graduate School

Copyright ©

by

Luis Sanchez

2013

Dedication

I dedicate my thesis to my parents

DIELECTRIC AND COMPLEX IMPEDANCE PROPERTIES OF
TETRAVALENT HAFNIUM (Hf^{4+}) INCORPORATED COBALT
FERRITE (CoFe_2O_4)

By

Luis Sanchez, M.A.S.E.

Thesis

Presented to the Faculty of the Graduate School of

The University of Texas at El Paso

in Partial Fulfillment

of the Requirements

for the Degree of

MASTER OF SCIENCE

Department of Metallurgical Engineering

The University of Texas at El Paso

December 2013

For Logo

Acknowledgements

My most heartfelt appreciation goes out to the individuals who have gone out of their way to help me accomplish this study. I could not have finished without the support, guidance, and attention they put to me.

I want to first of all express my gratitude to my thesis advisor and mentor Dr. C.V. Ramana, Associate Professor, Department of Mechanical Engineering, University of Texas at El Paso. My heart-felt sincere thanks for his time, parent-like discipline and guidance and, of course, for giving me the great opportunity to perform research under his guidance. I enjoyed working in this team.

I am profoundly grateful to Dr. Y.D. Kolekar, Visiting Assistant Professor working with Dr. Ramana's research team here at UTEP, for shaping me the 'true research student'; I never thought I could be. I deeply appreciated his valuable time and patience during his UTEP visiting period (summer, 2013).

I would like to thank the Department of Metallurgy and Mechanical Engineering for all their support during my graduate study completion at UTEP. I would also like to thank the faculty of the Metallurgy department for educating me in my graduate courses at UTEP. Lastly, I want to thank my family, whose tremendous support all along made this thesis possible. Without their love, support, and patience, I would not have been able to continue my study and complete this thesis work. Thank you family!

Abstract

The work presented in this thesis was carried out to understand the effects of tetravalent hafnium (Hf^{4+}) ion on the crystal structure and phase, surface morphology, electrical, dielectric and complex impedance properties of cobalt ferrite (CoFe_2O_4 ; CFO). Hafnium incorporated cobalt ferrite, $\text{CoFe}_{2-x}\text{Hf}_x\text{O}_4$, with $x = 0.00, 0.05, 0.075, 0.10, 0.15$ and 0.20 were prepared by the standard solid state ceramic synthesis method. X-ray diffraction (XRD) and scanning electron microscopy (SEM) characterizations were performed to determine the structural properties. Most important aspect of this study is to explore the dielectric and complex impedance properties as a function of variable temperature ($T=300$ - 1000 K) and frequency ($f=20$ Hz - 1 MHz). Room temperature and the temperature dependence of dielectric constant, loss factor, complex impedance, and the ac resistivity measurements enabled us to understand the effect of temperature and frequency on the electrical and dielectric properties on $\text{CoFe}_{2-x}\text{Hf}_x\text{O}_4$ and, thus, to derive structure-property relation.

X-ray diffraction (XRD) patterns for Hf-incorporated CFO confirm the formation of majority of CFO spinel [with space group $\text{Fd}\bar{3}\text{m}$ (227)] phase, in addition to the small amount of HfO_2 monoclinic [space group, $\text{P}121/c$ (14)] phase leading to formation of CFO-Hf composites. The lattice constant values derived from XRD for CFO-Hf were found to increase from 8.374 \AA ($x = 0.000$) to 8.391 \AA ($x = 0.200$). The lattice expansion is significant at the very first step of Hf-incorporation and then slows down with progressive Hf-incorporation. SEM imaging analysis indicates that Hf resides at the grain boundaries for CFO-Hf.

The dielectric constant (ϵ') of CFO-Hf is T -independent at $T < 450$ K, at which point increasing trend prevails. A grain bulk-boundary based two-layer model, where

semiconducting-grains separated by insulating-grain boundaries, satisfactorily accounts for ϵ - T (>450 K) variation. Correspondingly, electrical responses in impedance formalism are attributed to the grain and grain-boundary effects, respectively, which also accounts for the observed two dielectric-relaxations. The results demonstrate that the dielectric phenomena in CFO-Hf can be tailored by tuning Hf-concentration.

Table of Contents

Acknowledgements	vi
Table of Contents	ix
List of Tables	xi
Chapter 1: Introduction.....	1
1.1 Introduction to Ferrite Materials	1
1.2 Types of Ferrites	1
i) Garnet:.....	2
ii) Hexaferrite.....	3
iii) Orthoferrite	3
iv) Spinels	4
1.3 Cobalt Ferrite	7
1.4 Hafnium in Cobalt Ferrite.....	8
1.5 Importance of Hf incorporation in CFO	8
1.6 Objective of the study	9
Chapter 2: Materials and Methods	11
2.1 Synthesis.....	11
2.2. Crystal Structure and Phase Analysis - X-ray Diffraction (XRD)	11
2.3 Morphology - Scanning Electron Microscopy (SEM).....	13
2.4 Dielectric and Complex Impedance Spectroscopy.....	14
Chapter 3: Results and Discussion	17
3.1 Crystal Structure	17
3.2 Morphology and Chemical Composition	19
3.3 The Elemental Mapping Analysis	19
3.4 Dielectric Constant.....	21
3.4.1 Mesoscopic scale: Maxwell/Wagner/Sillars Polarization.....	21
3.5 Frequency Dependent Permittivity Measured at Room Temperature	22
3.5.1 Relaxation Time	23
3.5.2 Debye Model.....	24
3.6 Temperature Dependent Dielectric Constant	28
3.7 Temperature Dependent Dielectric Loss Tangent ($\tan \delta$)	30
3.8 Temperature dependent imaginary part of dielectric constant.....	33

3.9	Temperature Dependent AC Resistivity.....	35
3.10	Cole-Cole Plot.....	38
3.11	Complex Impedance Plots. Grain and Grain Boundary Contribution.....	40
Chapter 4: Conclusions		42
References.....		44
Curriculum Vita		50

List of Tables

Table 1: Arrangement of Metal Ions in the Unit Cell of a Ferrite $\text{MO} \cdot \text{Fe}_2\text{O}_3$	6
Table 2: Grain (g) and grain boundary (gb) electric response to Hf content.....	42

List of Figures

Figure 1.1 Crystal Structure of a Cubic Spinel Ferrite [50].....	5
Figure 1.2 Mineral (MgAl_2O_4) Spinel Structure [51]	6
Figure 2.1 Bruker D8 Advanced X-Ray Diffractometer	12
Figure 2.2 Braggs Diffraction Law Diagram [52].....	13
Figure 2.3 Scanning Electron Microscope (SEM)	14
Figure 2.4 Electrical/Dielectric Test Sample Holder.....	14
Figure 3.1 X-ray Diffraction Patterns.....	18
Figure 3.2 a) SEM image of CFO-Hf(0.200).....	19
Figure 3.3 EDS of Hafnium Incorporated Cobalt Ferrite Ceramics	20
Figure 3.4 Room temperature dielectric measurements	23
Figure 3.5 Spreading factor derivation plot	26
Figure 3.6 Calculated vs Experimental dielectric constant at room temperature	27
Figure 3.7 Temperature dependent dielectric constant for a given composition.....	29
Figure 3.8 Temperature dependent dielectric constant for a given frequency	30
Figure 3.9 Temperature dependent dielectric energy loss for a given composition.....	32
Figure 3.10 Temperature dependent dielectric energy loss for a given frequency.....	33
Figure 3.11 Temperature dependent imaginary part of dielectric constant for a given composition ...	34
Figure 3.12 Temperature dependent imaginary part of dielectric constant for a given frequency.....	35
Figure 3.13 Temperature dependent resistivity for a given composition	37
Figure 3.14 Temperature dependent resistivity for a given frequency	38
Figure 3.15 Complex impedance spectroscopy for pure CFO and CFO-Hf(0.200) with varying temperature	39
Figure 3.16 SEM images of CFO grain and grain boundaries.....	42

Chapter 1: Introduction

1.1 Introduction to Ferrite Materials

Ferrites are magnetic materials in which hematite (Fe_2O_3) or magnetite (Fe_3O_4) are the principal components. This material first came into commercial production in 1948. There are many applications as well as methods of making ferrites and the effects of such variables as porosity and grain size on their properties. The soft ferrites have a cubic crystal structure and the general formula $\text{MO} \cdot \text{Fe}_2\text{O}_3$, where M is a divalent metal such as Co, Zn, Mg, Mn, or Ni. All the commercial ferrites are mixed ferrites (solid solutions of one ferrite in another). Their densities are a little over 5 g/cm^3 , Curie temperatures range from about 300 to 600°C , and saturation magnetization (M_s) from about 100 to 500 emu/cm^3 (100–500 kA/m). Almost all of them have $\langle 111 \rangle$ easy directions of magnetization, low magnetocrystalline anisotropy, and low to moderate magnetostriction. Among the spinel ferrite family, cobalt ferrite (CoFe_2O_4 , referred to CFO throughout this thesis) has a high coercivity and the highest value of magnetostriction due to the highly anisotropic Co^{2+} ions, which make it useful for magnetostrictive sensors [1,2,3,4]. The ferrites are distinctly inferior to magnetic metals and alloys for applications involving static or moderate-frequency (power-frequency) fields, because they have M_s values less than a third of iron and its alloys and far lower permeability. But the exceptional fact about the ferrites is that they possess sufficiently high electrical resistivity in addition to the reasonably good magnetic properties. This means that they can operate with virtually no eddy-current loss at high frequencies, where metal cores, even those made of extremely thin tape or fine particles, would be useless. This fact accounts for virtually all the applications of soft ferrites [1].

1.2 Types of Ferrites

In general, there are four types of ferrites.

- i) Garnet, ii) Hexaferrite, iii) Orthoferrite, and iv) Spinel ferrite

i) Garnet:

The semiprecious stone garnet is actually a group of isomorphous minerals with a cubic structure. A typical composition is $\text{Mn}_3\text{Al}_2(\text{SiO}_4)_3$, but certain other divalent ions can be substituted for Mn^{2+} and similarly other trivalent ions for Al^{3+} . By substituting certain trivalent ions for the mixture of divalent (Mn^{2+}) and tetravalent (Si^{4+}) ions in the natural garnet, it is possible to make silicon-free garnets with the composition $3\text{M}_2\text{O}_3 \cdot 5\text{Fe}_2\text{O}_3$. The most magnetically interesting of these synthetic garnets are those in which M is yttrium (Y) or one of the rare earths from gadolinium (Gd) to lutetium (Lu), inclusive. These are all ferrimagnetic, but rather weakly so; saturation magnetization (σ_s) in the neighborhood of room temperature less than 10 emu/g or Am^2/kg . Yttrium-iron garnet ($\text{Y}_3\text{Fe}_5\text{O}_{12}$) commonly known as YIG, has a normal σ_s vs. T curve, but most of the rare-earth garnets exhibit a compensation point. YIG has important applications at very high frequency, particularly in the microwave region. The cubic unit cell is large, with a lattice parameter of $\sim 12.9 \text{ \AA}$, and it contains 160 atoms. Three crystallographically different kinds of sites exist, labeled conventionally as A, B, and C, and occupied as follows: 16 Fe^{3+} at A site, 24 Fe^{3+} at B site, and 24 M^{3+} at C site. The interaction between the Fe^{3+} ions at A and B sites is strongly antiparallel. In the rare-earth garnets, the moment of the rare-earth ions at C sites is antiparallel to the resultant moment of the Fe^{3+} ions. The Y^{3+} ion in YIG has no moment, so that the net moment of YIG is solely due to an unequal distribution of the same kind of ions (Fe^{3+}) in A and B sites, as in $\gamma\text{-Fe}_2\text{O}_3$. The garnets were extensively investigated and developed in the 1960s and 1970s during the creation of a nonvolatile computer memory and processor system based on moveable magnetized regions called bubble domains. A great deal of high-quality materials and engineering work was completed, but the system was not commercially successful and has disappeared [1]. They are used in microwave applications extremely narrow ferromagnetic resonance-absorption line [5].

ii) **Hexaferrite**

Barium ferrite has the formula $\text{BaFe}_{12}\text{O}_{19}$ with a hexagonal crystal structure, and fairly large uniaxial crystal anisotropy. Barium ferrite was developed into a commercial magnet material in 1952 in the Netherlands by the Philips Company, which called it Ferroxdure. A number of other trade names have been used, but with the expiration of patents, these materials are usually just called ceramic magnets or ferrite magnets. The composition is generally not specified, but better properties are observed for strontium instead of barium in the hexaferrite. The term “barium ferrite” can be understood to mean either material or a mixture. Sometimes the general term hexaferrite is used for both the materials. Hexaferrite may be used as fridge magnets, electric motors, loud speakers, and data storage [1]. They are interesting due to their recently discovered multiferroic behavior at room temperature [6]. However, much improvement is required in the development of these materials.

iii) **Orthoferrite**

Anti-ferromagnetism must be revised from its earlier definition and make it more general, to include the possibility that the spins of two sub-lattices may have any relation to each other as long as they form an ordered arrangement with no net magnetization. Slight deviations from ideal anti-ferromagnetism can also exist. In some Orthoferrite materials, spins of the two sub-lattices are not quite antiparallel but slightly tilted or “canted” out of the alignment. The result is a small net magnetization in one direction. From one point of view such materials are ferromagnetic; they are composed of domains, each spontaneously magnetized to a magnitude, and they show hysteresis. But they do not saturate, and in strong fields they exhibit susceptibility appropriate to their basic anti-ferromagnetism in the older literature this phenomenon is called parasitic ferromagnetism, and it was often attributed to a ferromagnetic impurity existing as particles of a second phase. It is now recognized as having

a more basic cause and is known as canted anti-ferromagnetism. Materials which show this behavior at room temperature include $\alpha\text{-Fe}_2\text{O}_3$ (hematite) and the rare-earth Orthoferrite. These have the general formula RFeO_3 , where R is yttrium or a rare earth ion. Their crystal structure is orthorhombic (three axes of unequal length at right angles to each other), and the spontaneous magnetization (σ_{sp}) is parallel to the c-axis (the $\langle 001 \rangle$ - axis of the cell), except in SmFeO_3 , where σ_{sp} is parallel to the a-axis. The combination of high magnetic frequencies with very large magneto optical effects makes the orthoferrites interesting subject for the study of laser-induced dynamics [1]. Orthoferrites are transparent, and can modify the polarization of a beam of light under the control of a magnetic field (Faraday rotation). This makes them potentially useful as optical sensors and actuators for use in optical communications [7].

iv) **Spinels**

These ferrites have the spinel structure and are sometimes called ferrosinels, because their crystal structure is closely related to that of the mineral spinel, $\text{MgO} \cdot \text{Al}_2\text{O}_3$. The structure is face centered cubic. Eight formula units or a total of $8 \times 7 = 56$ ions exists per unit cell. The large oxygen ions (ionic radius $\sim 1.3 \text{ \AA}$) are packed quite close together in a face-centered cubic arrangement; the much smaller metal ions ($0.7\text{-}0.8 \text{ \AA}$) occupy the spaces between them. These spaces are of two kinds. One is called a tetrahedral (or A site), because it is located at the center of a tetrahedron whose corners are occupied by oxygen ions (Fig. 1.1c). The other is called an octahedral (or B site), because the oxygen ions around it occupy the corners of an octahedron (Fig. 1.1b).

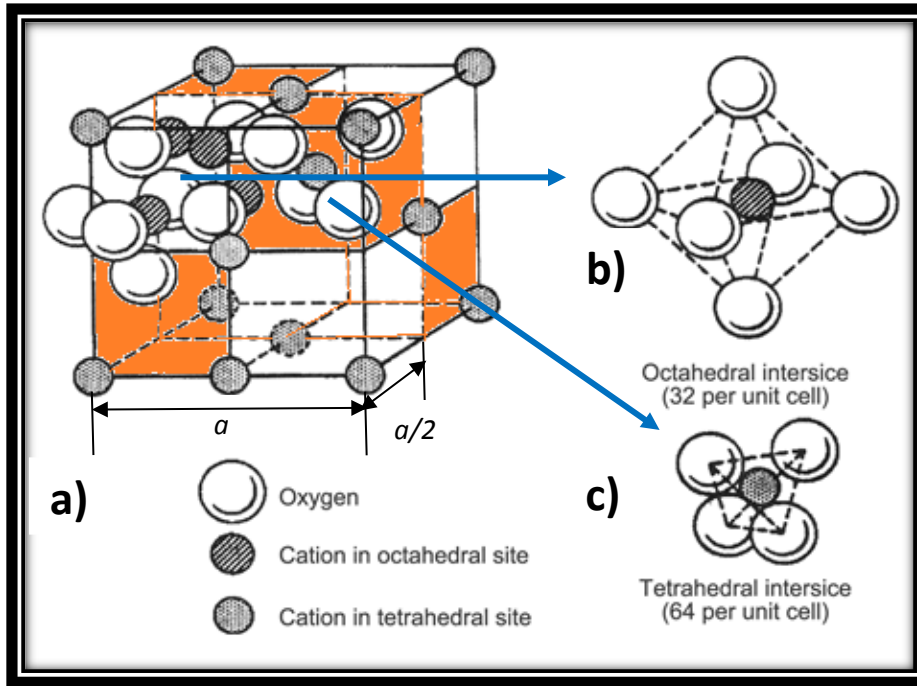


Figure 1.1 Crystal structure of a cubic spinel ferrite [50]

The crystallographic environments of the A and B sites are distinctly different. The unit cell contains 56 ions, a two-dimensional drawing of the complete unit cell is too cluttered to be useful. Instead, we can consider a unit cell of edge ' a ' to be divided into eight octants, each of edge ' $a/2$ ', as shown in Fig. 1.1a. The four orange octants have identical contents, and so do the four white octants. The contents of the two upper-left octants are shown in Fig. 1.1b and 1.1c. One tetrahedral site occurs at the center of the upper-right octant, and the other tetrahedral sites are at some but not all octant corners. Four octahedral sites occur in the upper-left octant; one is connected to six oxygen ions, two of which, are in adjacent octants backside and bottom. Similarly, in tetrahedral, the oxygen ions are arranged in the same way in all octants. Not all of the available sites are actually occupied by the metal ions. Only one-eighth of the A site and one-half of the B site are occupied, as shown in Table 1. In the MgAl_2O_4 mineral spinel, the Mg^{2+} ions are present at A site and the Al^{3+} ions are at B site [1].

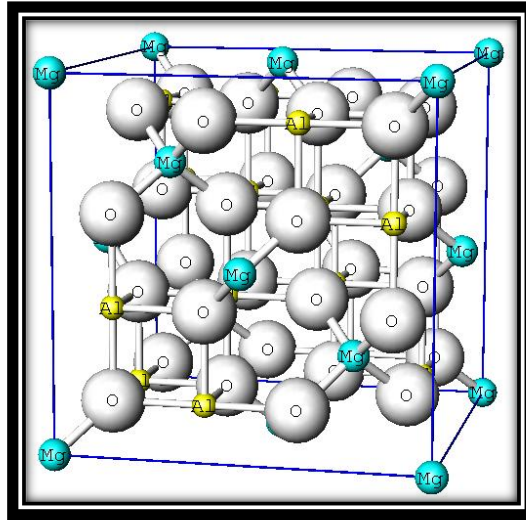


Figure 1.2 Mineral (MgAl₂O₄) Spinel Structure [51]

All spinel ferrites $\text{MO} \cdot \text{Fe}_2\text{O}_3$ have exactly the same structure shown in Figure 1.2, with M^{2+} at A site and Fe^{3+} at B site. This is called the normal spinel structure. Both zinc and cadmium ferrites have this structure and they are both nonmagnetic, i.e., paramagnetic. Many other ferrites, however, have the inverse spinel structure where the divalent ions occupy the B site and the trivalent ions are equally divided between A and B sites. The divalent and trivalent ions normally occupy the B sites in a random fashion i.e., they are disordered. Iron (Fe), cobalt (Co), and nickel (Ni) ferrites exhibit inverse structure and are ferromagnetic [1].

Table 1: Arrangement of metal ions in the unit cell of a ferrite $\text{MO} \cdot \text{Fe}_2\text{O}_3$

Name of site	Number of available sites	Number of occupied sites	Occupants	
			Normal spinel	Inverse spinel
Tetrahedral (A)	64	8	8M^{2+}	8Fe^{3+}
Octahedral (B)	32	16	16Fe^{3+}	$8\text{Fe}^{3+} \quad 8\text{M}^{2+}$

The high electrical resistivity and the outstanding magnetic properties make the spinel ferrites excellent core materials for power transformer in electronic and telecommunications applications [8]. Magnetic spinels can also be characterized for good chemical stability, mechanical hardness and high coercivity and thus make them excellent candidates for nonvolatile memory device applications based on their resistive switching performance [7,8,24,25,26,30].

The distribution of the divalent ions between A and B sites in some ferrites can be altered by heat treatment; it may depend, for example, on whether the material is quenched from a high temperature or slowly cooled [1]. Ferrites can be prepared with two or more different kinds of divalent ion, e.g. (Ni, Zn)O·Fe₂O₃. This is called a mixed ferrite. Most of the cubic ferrites used commercially are mixed ferrites [1].

1.3 Cobalt Ferrite

Cobalt ferrite (CoFe₂O₄) is a spinel ferrite with a chemical composition of AB₂O₄. Among the three types of spinel ferrites, cobalt ferrite has an inverse spinel structure which has a face centered cubic, closely packed arrangement of oxygen ions with the Co²⁺ occupying the octahedral sites and the Fe³⁺ ions equally distributed among the tetrahedral and octahedral sites. Passionate investigations on ferrite materials are paving the way to develop magnetoresistive random access memory (RAM). Other applications of these materials take place in electrochemical, optoelectronic, magnetic, electronic, ferro-fluid, semiconductor, and anti-cancer drug delivery industries [11-27]. Cobalt ferrite is well known for its good dielectric properties, moderate saturation magnetization, large magnetocrystalline anisotropy, chemical stability, mechanical hardness, and high coercivity [7,10,12,13,16,17,21,22].

The dielectric and electrical properties of ferrites will vary due to particle/atomic size, morphology, as well as cation distribution, which all depend on the method of synthesis

[10,31-42]. Previous reports [4, 30, 31, 32], demonstrate an increase in the dielectric constant, saturation magnetization, and conductivity and a decrease in the Curie temperature with a given addition of Mn ions in spinel ferrites. The enhanced property results of larger ion substitutions contributed to numerous investigations on the fabrication and synthesis of cobalt ferrite ceramics including ball milling [4], a ceramic method by firing [33], impregnation [29], reverse micelles, hydrothermal methods [31,32,34], a polymeric precursor [35], sol-gel [17,39], and a polyol [31] method.

1.4 Hafnium in Cobalt Ferrite

The ionic size of hafnium (Hf^{4+}) ions (0.76Å) and cobalt ions (0.735Å) is considerably larger than that of iron ions (0.645Å) [Shannon and Prewitt]. The inclusion of hafnium into cobalt ferrite may produce the lattice distortions in the spinel structure and accordingly some previous reports have shown that this distortion causes changes in the dielectric and electrical properties of the cobalt based ceramic compounds [8,43]. Hafnium is a promising alloying component having all the desirable qualities of high k materials and its chemical stability is an advantage [44]. Its high density (9.68 g/cm³) makes it resistive to impurity diffusion [44]. To the best of our knowledge, there has been only one case reported by Wells and Ramana [11] where the hafnium is incorporated into cobalt ferrite and the structural, chemical, and room temperature (RT) dielectric property effects were observed.

1.5 Importance of Hf incorporation in CFO

As discussed by T.M. Meaz et al. [45], during the sintering process, at high temperatures, Fe^{2+} ions arise from the partial reduction of Fe^{3+} ions. Fe^{2+} ions prefer to occupy the B-site, while Fe^{3+} can occupy A- and B-sites [45]. Also, Co^{2+} ions may be oxidized to Co^{3+} during sintering as well. In small Hf concentrations, Co ions prefer to occupy at B-site [44]. Thus, it is expected that the conduction process occurs as a result from

the electron exchange between Fe^{2+} and Fe^{3+} ions (n type charge carriers) and hole transfer between Co^{2+} and Co^{3+} ions (p-type charge carriers) at octahedral sites [44]. We expect that Hf^{4+} ions may occupy B-site when it is added in a small amount (up to 0.075), with further increase of Hf ion content; it will occupy the A-site. The presence of Hf ions at B-site will act as electrostatic trap for the electron exchange between Fe^{2+} and Fe^{3+} ions by forming electrostatic bonds with Fe^{2+} . Therefore, when hafnium incorporation becomes more than 0.075, the presence of Hf ions at A-site may allow an increase in the conductivity by increasing the chance of formation of Fe^{2+} needed for the hopping mechanism, which is in good agreement with the observed behavior of the ac resistivity with Hf. Therefore, the behavior of the resistivity with Hf in this system suggested that Hf ions play a major role in the conduction process.

Complimentary with the last paragraph, Hf^{4+} ions may go to the Fe^{3+} site in cobalt ferrite grains, when Hf present in small amounts (<0.075 wt%). At higher Hf concentrations, Hf^{4+} ions reach saturation in cobalt ferrite and instead begin to settle at grain boundaries. Due to this developed morphology, the contribution to the polarization effects from the grain boundaries strongly increase.

1.6 Objective of the study

The goal of the present work is to provide a continuing extract on the dielectric and electrical properties of hafnium incorporated cobalt ferrite in the frequency range (F : 20 Hz- 1 MHz) and over the temperature range (T : 25 °C to 700 °C). We examine the dielectric constant and dielectric loss as a function of temperature and frequency. The resistance (R/Z') and reactance (X/Z'') were measured at room temperature and at various fixed temperatures by varying the frequency from 20 Hz to 1 MHz were. These measurements were used to obtain the temperature dependent complex impedance plots and depict how the grains and the grain

boundary play an important role in the capacitance enrichment and also on the conduction.

The specific research objectives of this thesis work are:

1. Synthesize tetravalent Hf incorporated cobalt ferrite ceramics with variable Hf content.
2. Evaluate the frequency ($f=20\text{ Hz} - 1\text{ MHz}$) and temperature ($T=300-973\text{ K}$) dependent dielectric properties of hafnium incorporated cobalt ferrite.
3. Understand the mechanisms responsible for the dielectric behavior, dielectric relaxation properties, and loss factor associated with CFO-Hf ceramics.
4. Propose a model to account for electrical responses in impedance formalism especially using the grain and grain-boundary effects (if present).
5. Derive a correlation between structure, dielectric and impedance properties of CFO-Hf ceramics.

Chapter 2: Materials and Methods

2.1 Synthesis

Pure cobalt ferrite (CFO), CoFe_2O_4 and Hf integrated CFO (CFO-Hf) samples were prepared by the standard solid state chemical reaction method. The powders in the mixture consists of Cobalt (II) Oxide (CoO <10 microns 99.5% pure), Iron (III) Oxide (Fe_2O_3 - 0.3 micron 99.95% pure), and Hafnium (IV) Oxide (HfO_2 ; 99.95% pure; from Alfa Aesar). These starting materials were mixed in a required ratios to produce CoFe_2O_4 , $\text{CoFe}_{1.95}\text{Hf}_{0.05}\text{O}_4$, $\text{CoFe}_{1.925}\text{Hf}_{0.075}\text{O}_4$, $\text{CoFe}_{1.9}\text{Hf}_{0.1}\text{O}_4$, $\text{CoFe}_{1.85}\text{Hf}_{0.15}\text{O}_4$, and $\text{CoFe}_{1.8}\text{Hf}_{0.2}\text{O}_4$. After obtaining these desired CFO and CFO-Hf compositions, the powders were mixed in a pestle and mortar for three hours using ethanol as a medium. Then each batch was pressed into one large disc shape pellet in a Carver press at 2.5 tons, individually calcined at 1200°C for 10 hours, and after cooling they were crushed in a pestle and mortar again for an hour then pressed with 6 tons of pressure into small disc shaped pellets of roughly 0.18-0.21cm in thickness (t) and between 0.3125-0.3131cm in diameter. Finally, they were sintered at 1300°C for 12 hours.

2.2. Crystal Structure and Phase Analysis - X-ray Diffraction (XRD)

The structural characterization was performed with the utilization of a Bruker D8 Advanced X-Ray Diffractometer (XRD) (see Figure 2.1). The crystal structure of preferred crystallographic orientation, average crystallite size, and phases were determined from the XRD analysis.



Figure 2.1 Bruker D8 Advanced X-Ray Diffractometer

In the XRD technique, a parallel beam of X-rays incident on the sample surface, which then diffracts from the first and second atomic lattice layers capturing them in the detector (see figure 2.2). The detector sends the angle at which the X-ray was received which correlates it to the inter-planar atomic distance (d-spacing). The d-spacing is calculated using Bragg's Law shown in eqn (1).

$$n\lambda = 2d \sin(\theta) \dots\dots\dots (1)$$

Where λ is the wavelength of incident X-rays, d is the inter-planar spacing, and θ is Bragg's angle. The X-ray was produced by a copper target thus giving off $\text{CuK}\alpha$ radiation ($\lambda=1.54056$) at room temperature.

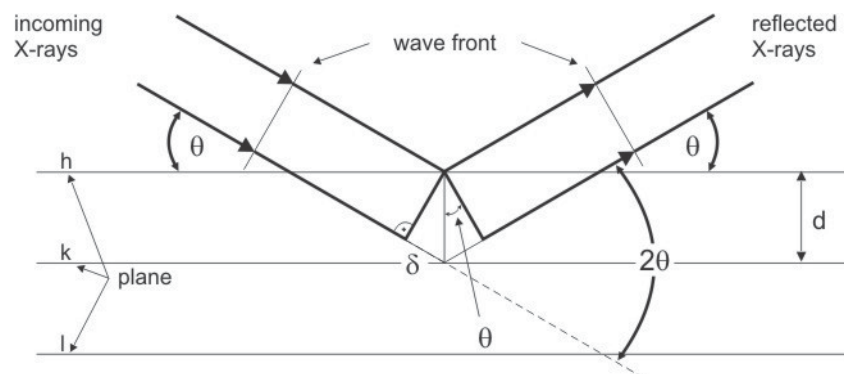


Figure 2.2 Braggs Diffraction Law Diagram [52]

The patterns given by XRD are in the form of peaks whose height may represent a quantitative measure of the amount of grains which are oriented in a certain crystallographic orientation. In the present work, CuK_α radiation of wavelength 1.54058 \AA was employed to obtain XRD patterns of the CFO-Hf ceramics. Measurements were made in the 2θ range from 20° to 80° with an increment of 0.05° , and at a scan rate of 1 degree per minute.

2.3 Morphology - Scanning Electron Microscopy (SEM)

Principle of Operation

An electron beam incident on the sample surface and ejects the weakly bonded electrons called secondary electrons (SE). These electrons have low energy and can be detected by the detector to produce an SEM image of the sample surface up to 1 micrometer in depth. The low energy SE's can be affected by the electromagnetic field. To avoid charge build up on the sample surface, the sample must be properly attached to a conductive copper tape strip or a coating of graphite. The SEM (model: Hitachi S-4800) available at UTEP is shown in Figure 2.3.



Figure 2.3 Scanning Electron Microscope (SEM)

To produce the beam, electrons are thermionically emitted from a cathode tungsten filament and drawn to an anode. The electron beam energy can be employed in a range from 0.5 KeV to 40 KeV. Two condenser lenses in the vacuum chamber are used to focus the beam to a surface area of 1 nm to 5 nm in diameter. The path of the beam on the sample surface follows a raster scan pattern. Sweeping from left to right, it blanks as it rapidly moves back to the left position and scans the next line downwards. When the primary electrons from the beam hit the sample, its energy is high. The high energy beam loses its energy by random scattering and absorption. Due to the low energy of the excited secondary electrons, they can be detected by the SE detector and produce the SEM image.

2.4 Dielectric and Complex Impedance Spectroscopy

Pellets in the form of disc were placed between two flat, parallel silver foils (electrodes). The smooth surfaces of the CFO/CFO-Hf samples were coated with high purity

silver paste for good Ohmic conduction. An electric field with a potential of 1 Volt is applied through the sample between the silver electrodes. This setup can be considered electrically equivalent to a capacitance C_p in parallel with a resistance R_p [20].



Figure 2.4 Electrical/Dielectric Test Sample Holder

The dielectric constant, loss, the ac resistivity and conductivity were determined using the following formulas:

$$\epsilon' = \frac{11.29 \times C_p \times t}{A} \dots \dots \dots (2)$$

$$\tan \delta = \frac{\epsilon''}{\epsilon'} \dots \dots \dots (3)$$

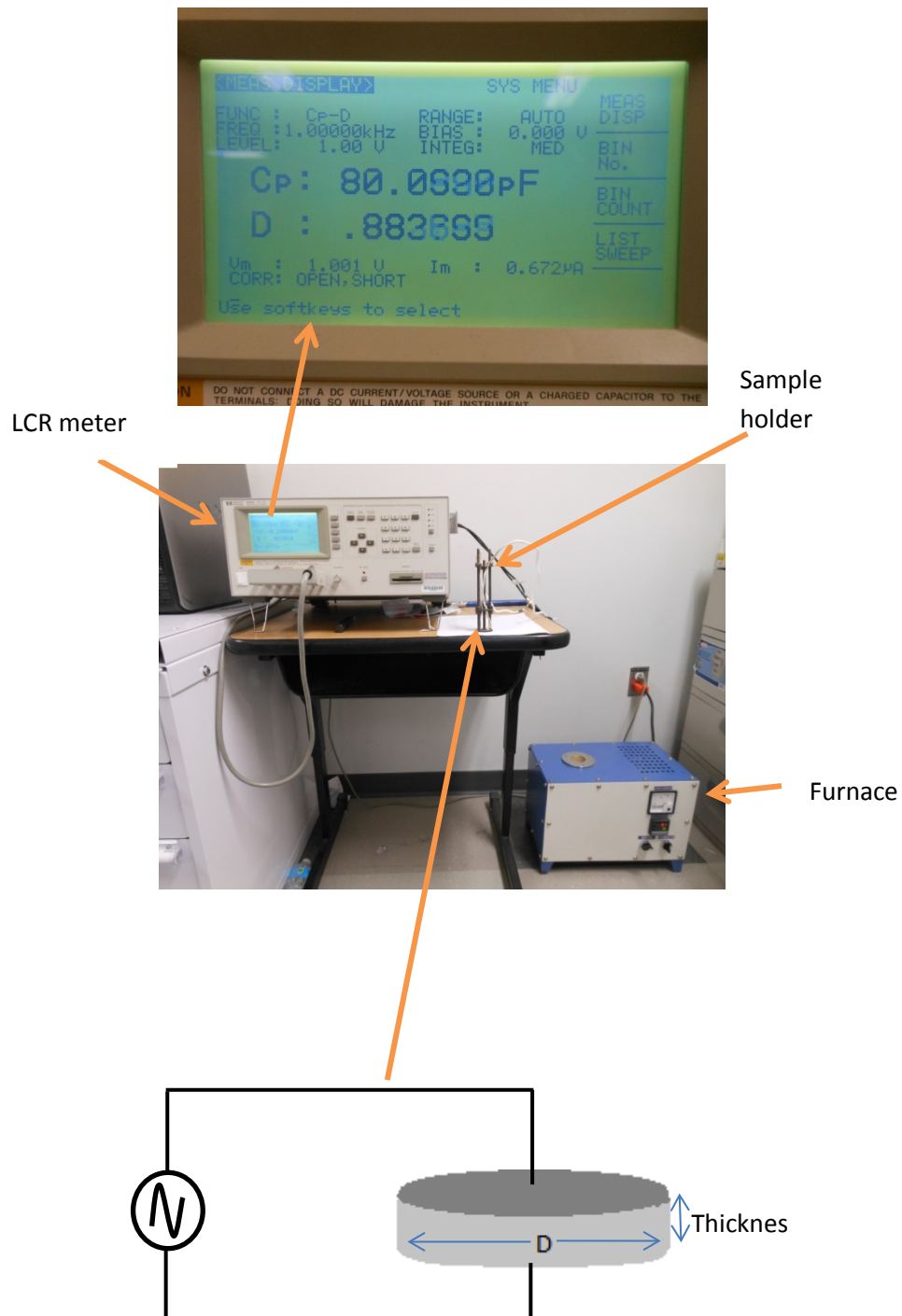
$$\rho_{ac} = \frac{R \times A}{t} \dots \dots \dots (4)$$

$$\sigma_{ac} = \frac{1}{\rho} \dots \dots \dots (5)$$

where C_p is the capacitance in picofarads, t is the thickness of the sample (cm), A is the cross sectional area of the sample (cm^2), $\tan \delta$ is the dissipated energy loss, ϵ'' is the imaginary part of the dielectric constant (loss factor), ϵ' is the real part of the imaginary constant, R is the

resistance in Ohms, ρ is the resistivity (Ohm-cm), σ is the conductivity (1/Ohm-cm). These values were attained using an HP 4284A LCR meter.

On Site Schematic



Chapter 3: Results and Discussion

3.1 Crystal Structure

X-ray diffraction (XRD) patterns of CFO-Hf composites are shown in Fig. 3.1a. XRD data confirm the spinel phase, with space group $Fd\bar{3}m$ (227), for CFO ($x=0.000$). A small amount of HfO_2 phase can be seen for CFO-Hf composites. No other phases were detected confirming the successful preparation of CFO-Hf with spinel phase. However, peak shift is noted in CFO-Hf compared to CFO (Fig. 3.1b). The intensity of the additional peaks due to HfO_2 increases with increasing x (Fig. 3.1c). The lattice constant values derived from XRD for CFO-Hf were found to increase from 8.374 Å ($x=0.000$) to 8.391 Å ($x=0.200$). The lattice expansion is large even for a very small amount of Hf ($x=0.050$) at the very first step. The lattice constant change then slows down with x . The significant lattice expansion in CFO-Hf can be attributed to the ionic size difference in the Hf^{4+} ions compared to Fe^{3+} ions. The ionic size of Hf^{4+} (0.83 Å) is greater than that of Fe^{3+} (0.67 Å) and induces a lattice distortion upon Hf-incorporation at Fe lattice sites in CFO. Most importantly, in order to confirm the HfO_2 incorporation is carried out efficiently and sintering was performed to the best possible extent, the density of the ceramics is calculated from the XRD data. The density obtained from XRD calculations for pure CFO is 5.21 g/cm³, which is in agreement with the standard density (5.27 g/cm³) for cobalt ferrite. The density values calculated for CFO-Hf composites from XRD indicate an increasing trend from 5.21 to 5.80 g/cm³ with increasing HfO_2 concentration (x from 0.0 to 0.2). The increased density values, thus, confirm the incorporation of Hf into CFO and completeness of the sintering process as well. Furthermore, the EDS data as shown and discussed in section 3.2 also confirmed the increasing Hf concentration in the samples.

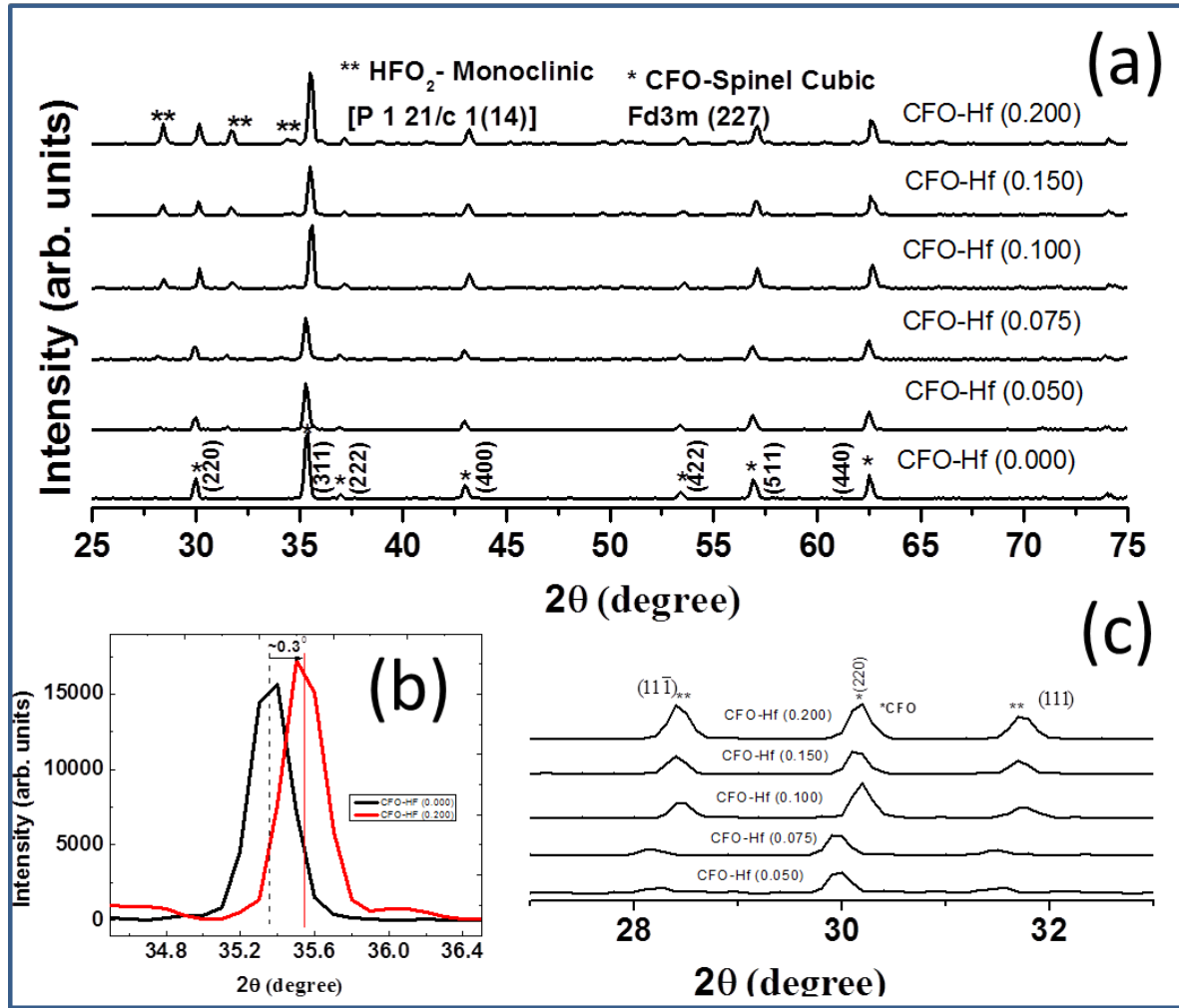


Figure 3.1 (a) XRD patterns (slow scans) of the CFO-Hf ceramics as a function of x . The data indicate that the CFO-Hf crystallize in inverse spinel structure. Formation of secondary HfO₂ phase can be seen with increasing Hf-content. Indexing of the peaks due to CFO and HfO₂ are as labeled. (b) The (311) peak of CFO-Hf ($x=0.200$) compared to CFO ($x=0.000$). Peak shift with Hf incorporation is evident. (c) Expanded region of monoclinic HfO₂ peaks, which are dominant with increasing x .

3.2 Morphology and Chemical Composition

The SEM images from the different samples are shown below in Figure 3.2. The crystallites are seen to be evenly distributed in the scan. Also, smooth grain boundaries are evident.

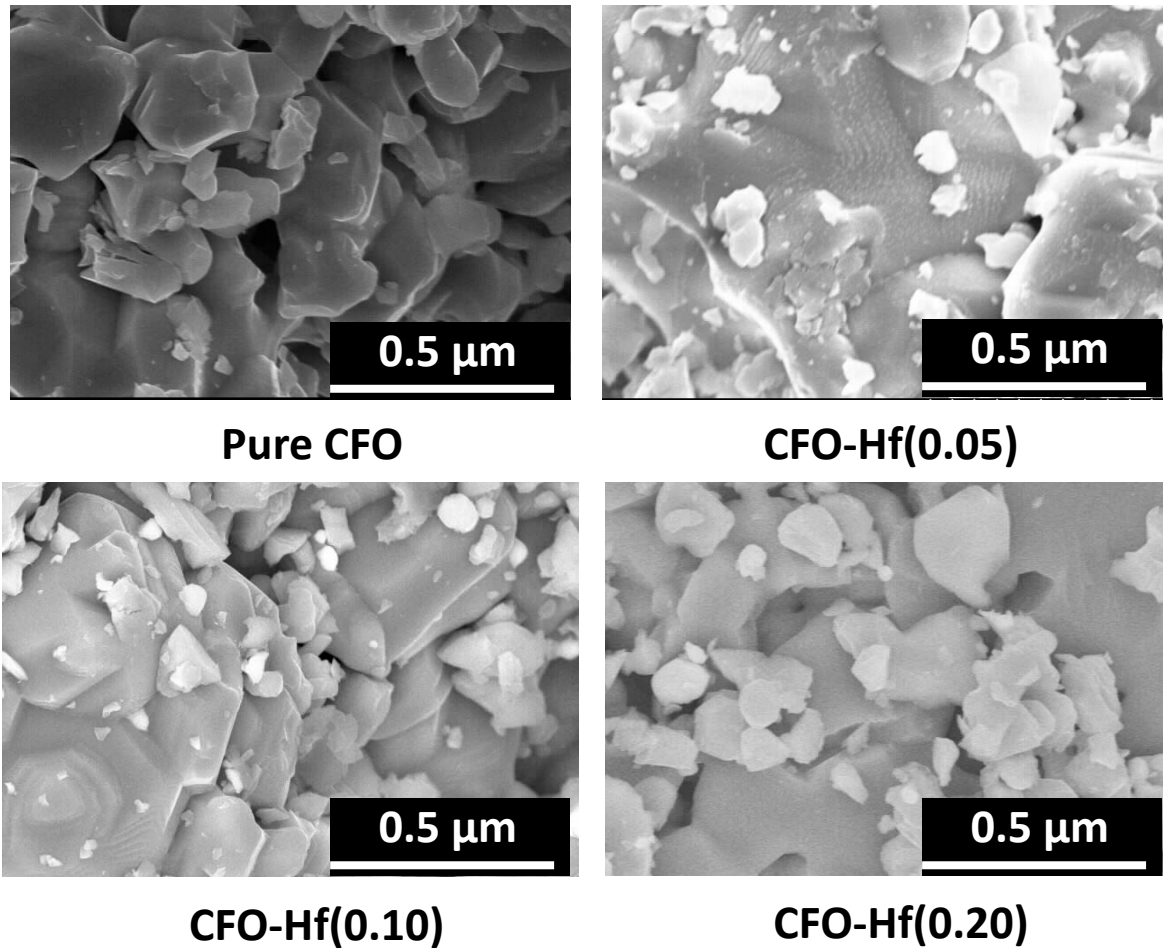


Figure 3.2 SEM images of Hf-incorporated cobalt ferrite ceramics

3.3 The Elemental Mapping Analysis

The EDS scans show a qualitative balance of the elements in the samples based on the x-rays emitted by each ion when struck by an electron beam, which is unique to the generating element [31,33]. The scans are shown in the figure below as a function of Hf concentration.

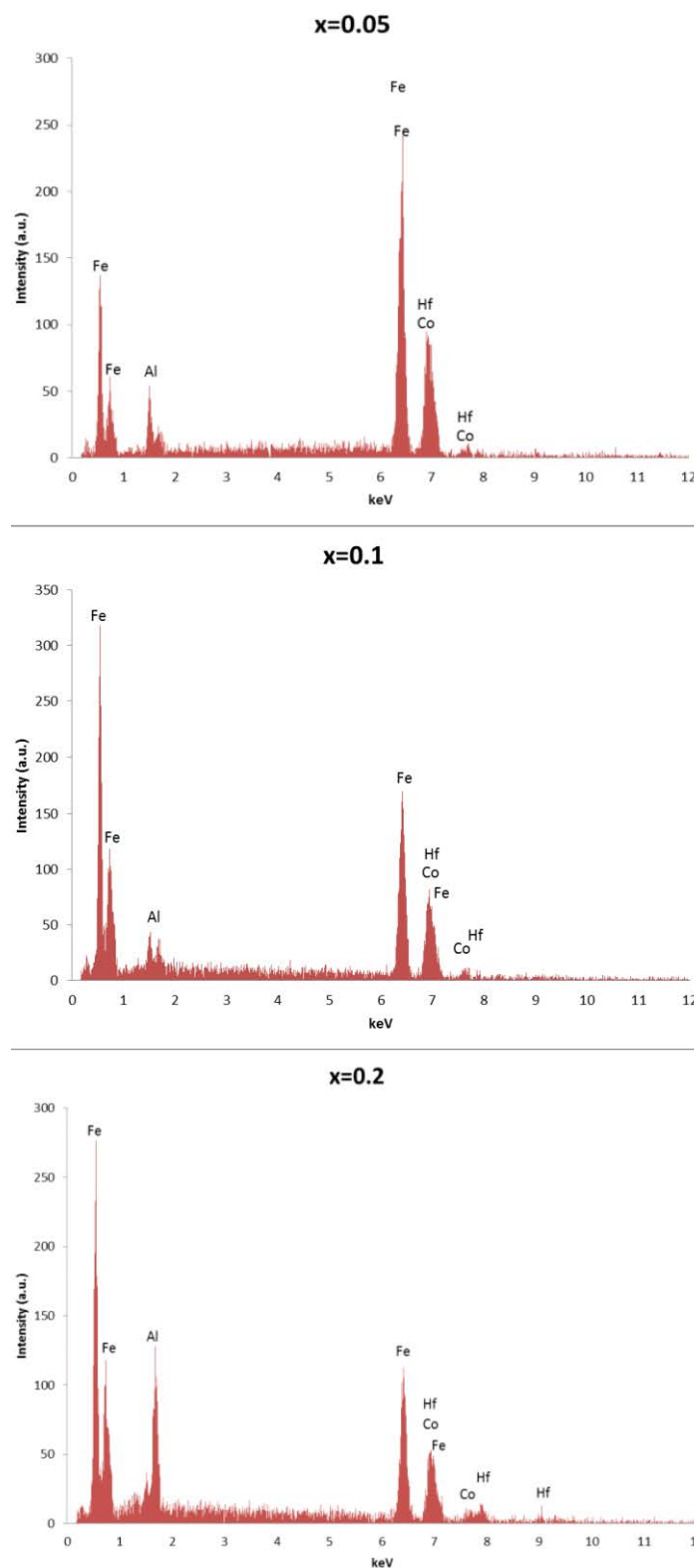


Figure 3.3 (a) EDS data of Hf-incorporated cobalt ferrite ceramics

The materials are stoichiometric and homogeneous, being evenly distributed. The x-ray lines for Fe K α , Co K α , O K α , La L α and Co L α appear on the graph at their proper energy positions. Since

there is no La in the sample, these are all for Fe, Co, Hf, and O. C and Al also appear due to the carbon tape and Al holder used in the scan. The scan shows great purity in the samples, and proper increase in concentration of Hf in the high concentration samples.

3.4 Dielectric Constant

The permittivity (dielectric constant) is a measure of how much electric flux is produced in a medium per unit charge. With an increase in permittivity, more electric flux occurs due to polarization effects. Permittivity is associated to the ease in which a dielectric material polarizes in response to an electric field. The complex dielectric function $\epsilon^*(\omega)$ in its dependence on angular frequency (external electrical field) and temperature originates from different processes: i) microscopic fluctuations of molecular dipoles (rotational diffusion) [10], ii) propagation of mobile charge carriers (translational diffusion of electrons, holes, or ions), and iii) separation of charges at interfaces which gives rise to an additional polarization. The latter can take place at inner dielectric boundary layers (Maxwell/Wagner/Sillars-polarization on a mesoscopic scale and/or at the external electrodes contacting the sample (electrode polarization) on a macroscopic scale [21].

3.4.1 Mesoscopic scale: Maxwell/Wagner/Sillars Polarization

For inhomogeneous materials, in our case a polycrystalline ceramic, the influence of Maxwell-Wagner (M-W) interfacial polarization is an important mechanism and must be considered when pursuing an investigation on the dielectric behavior of a ceramic composite or system. According to the M-W two layer model, conductive grains are separated by poorly conducting grain boundaries. The electron exchange between Fe^{2+} and Fe^{3+} is due to the displacement of ions in the direction of the applied field which determines the polarization in ferrites [43]. At internal grain boundaries or interface boundaries, the movement of charges can be restricted thus giving rise to Maxwell/Wagner type interfacial polarization.

3.5 Frequency Dependent Permittivity Measured at Room Temperature

The dielectric constant decreases strongly with increasing frequency, particularly in the lower frequency range. This can be explained on the basis of M-W interfacial polarization. At low frequencies, the natural oscillation (lattice vibration) of the system is in phase with the applied frequency and all types of polarizations are present i.e., $P_{\text{total}} = P_i + P_d + P_a + P_e$, where the subscripts i, d, a and e represent the interfacial (or space charge), dipolar, atomic (or ionic), and electronic contributions, respectively [28]. The response time for electronic and atomic polarization is so short and can be assumed to be negligible for all frequencies from 0 to about 10^{12} Hz, so we can group these two polarizations as $P_\alpha = P_e + P_i$. These two types of polarization can be considered to follow instantaneously the excitation field frequency without time lag; in other words, P_α and frequency can be considered to be in phase [48]. However, as the frequency of the AC field is increased, there comes a point where the natural oscillation of the interfacial and dipolar contributing species, in other words the electron exchange $\text{Fe}^{2+} \leftrightarrow \text{Fe}^{3+}$ lags behind the frequency of the applied field thus comes out of phase and the dielectric constant of all samples merge to a constant value at 1 MHz in this case.

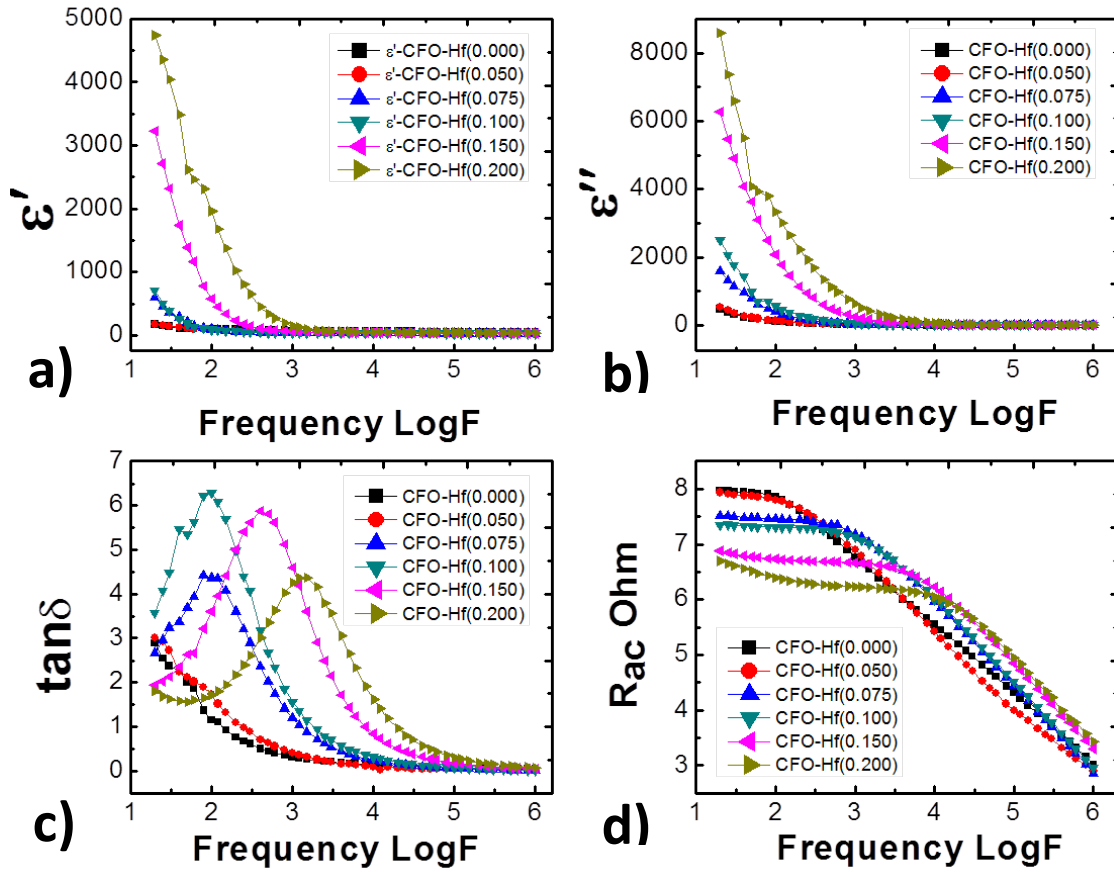


Figure 3.4 Room temperature dielectric data of Hf-integrated cobalt ferrite ceramics. The data shown are as a function of variable composition of Hf in cobalt ferrite. (a) Frequency variation of the real part of the dielectric constant; (b) Frequency variation of the imaginary part of the dielectric constant; (c) Frequency variation of the dielectric losses; (d) Frequency variation of the ac electrical resistance

3.5.1 Relaxation Time

The time required for orientational, hopping, or space charge polarization and depolarization is quite long and varies in a wide range, depending on the dielectric systems. Such polarization processes are sometimes referred to as relaxation processes because they involve a relaxation time. A relaxation phenomenon occurs when restoring action tends to bring the excited system back to its original equilibrium state [47].

Relaxation time is the time required for the permanent dipoles (positive and negative charges of opposite sign but equal magnitude) to reorient (relax) according to the change in the externally applied electric field.

Relaxation processes are characterized by a peak in the imaginary part and a step-like decrease of the real part of the complex dielectric function with increasing frequency. In non-ohmic conduction or polarization effects (at inner boundaries or external electrodes) the dielectric constant increases with decreasing frequency as seen in (Fig. 3.7) [47].

3.5.2 Debye Model

Dielectric relaxation processes are usually analyzed using model functions. The well-known and studied Debye function is the most important function useful to model the dielectric constant variation. We have used Debye model to confirm the experimentally observed frequency dependent dielectric constant at room temperature. The modified Debye function used for the frequency dependent dielectric constant [47] is given below. Other equations employed to model the dielectric data are also given below.

Debye equation

$$\epsilon^*(\omega) = \epsilon_{\infty} + \frac{\epsilon_l - \epsilon_{\infty}}{1 + (\omega\tau)} \dots\dots\dots (6)$$

Cole-Cole equation

$$\epsilon^*(\omega) = \epsilon_{\infty} + \frac{\epsilon_l - \epsilon_{\infty}}{1 + (\omega\tau)^{1-\alpha}} \dots\dots\dots (7)$$

Davidson-Cole equation

$$\epsilon^*(\omega) = \epsilon_{\infty} + \frac{\epsilon_l - \epsilon_{\infty}}{1 + (\omega\tau)^{\beta}} \dots\dots\dots (8)$$

H-N equation

$$\epsilon^*(\omega) = \epsilon'_{\infty} + \frac{\epsilon'_l - \epsilon'_{\infty}}{1 + (\omega\tau)^{\beta(1-\alpha)}} \dots\dots\dots (9)$$

Modified Debye Equation

$$\varepsilon'(\omega) = \varepsilon'_\infty + \frac{\varepsilon'_l - \varepsilon'_\infty}{1 + (\omega\tau)^{2(1-\alpha)}} \dots\dots\dots (10)$$

where α and β are parameters with $0 < \alpha < 1$ and $0 < \beta < 1$. $\varepsilon^*(\omega)$ is the complex permittivity, $\varepsilon'_l - \varepsilon'_\infty$ is the dielectric relaxation strength; ε'_l being the static (low frequency permittivity) and ε'_∞ being the permittivity at the high frequency limit. τ is the Debye average relaxation time, α is the spreading factor, and the field's angular frequency ω is also expressed as $\omega = 2\pi \times f$ with f being the linear frequency of the applied field.

Using the modified Debye equation we can derive theoretical dielectric constant as a function of frequency. All the values in (equation 10) were given or can be calculated from the experimental dielectric data except for α . However, the plots shown in (Figure 3.5) show a line with slope equal to $1-\alpha$. We can solve for α from the following plots.

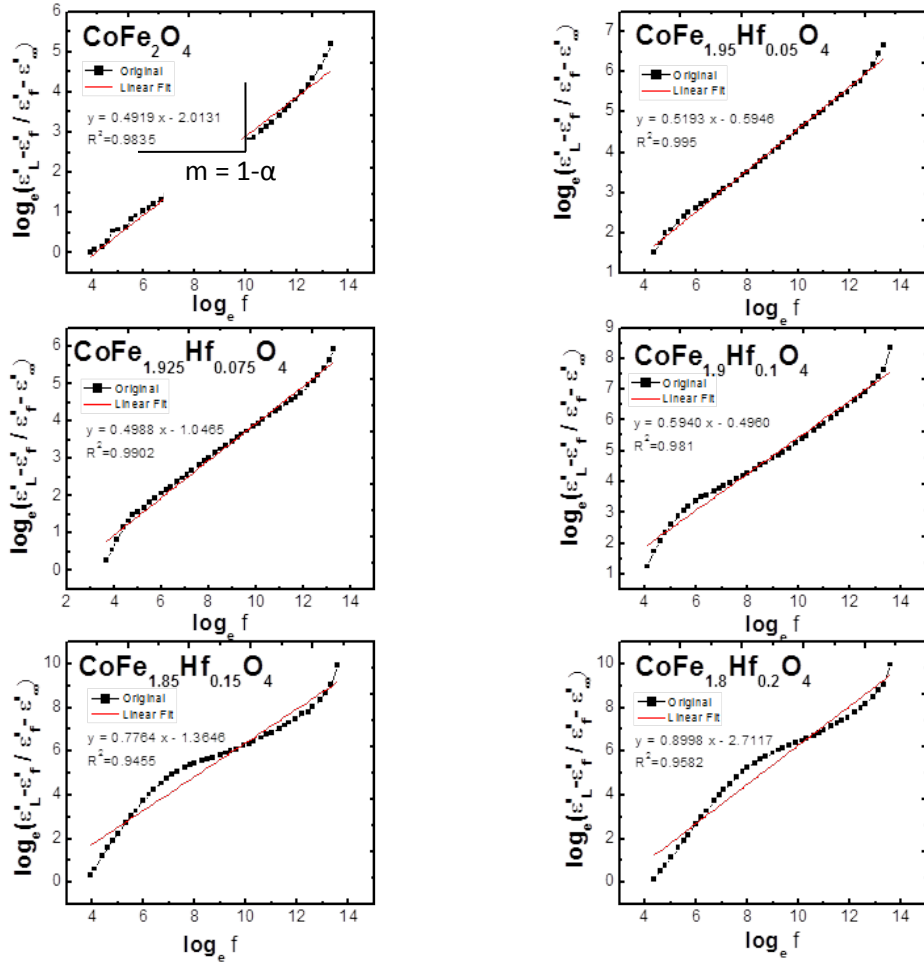


Figure 3.5 Spreading factor derivation plot

We then solved for τ in equation 10 in the following way:

$$\epsilon^*(\omega) = \epsilon'_\infty + \frac{\epsilon'_l - \epsilon'_\infty}{1 + (\omega\tau)^{2(1-\alpha)}}$$

$$\epsilon^*(\omega) - \epsilon'_\infty = \frac{\epsilon'_l - \epsilon'_\infty}{1 + (\omega\tau)^{2(1-\alpha)}}$$

$$1 + (\omega\tau)^{2(1-\alpha)} = \frac{\epsilon'_l - \epsilon'_\infty}{\epsilon^*(\omega) - \epsilon'_\infty}$$

$$(\omega\tau)^{2(1-\alpha)} = \frac{\epsilon'_l - \epsilon'_\infty}{\epsilon^*(\omega) - \epsilon'_\infty} - 1$$

$$\tau = \frac{1}{\omega} \times \left[\frac{\epsilon'_l - \epsilon'_\infty}{\epsilon^*(\omega) - \epsilon'_\infty} - 1 \right]^{\frac{1}{2(1-\alpha)}}$$

The average relaxation values for all ceramics with variable Hf content were obtained. With all values determined, we were able to plug them into equation 10 and obtain the calculated real part of dielectric constant with varying frequency. The plots shown in Fig. 3.6 illustrate the calculated and experimentally observed dispersion in dielectric constant.

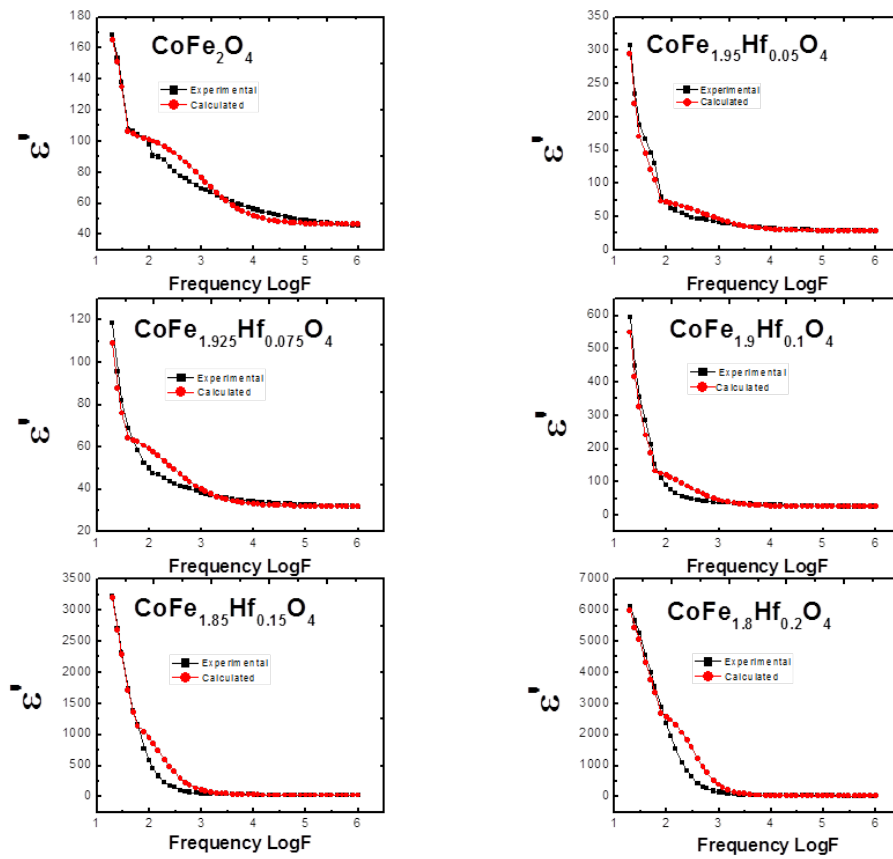


Figure 3.6 Calculated vs experimental RT dielectric constant

3.6 Temperature Dependent Dielectric Constant

As seen in (Fig. 3.7a-d), the dielectric constant increases with temperature up to the transition temperature (T_i), then decreases beyond it. Generally, the temperature dependent behavior of dielectric constant for ferrites is influenced by the four types of polarization (P_i , P_d , P_a , and P_e). The quick initial increase in dielectric constant with temperature is largely due thermally activated charge carriers in congruence with interfacial and dipolar polarization, which are strongly temperature dependent [8,46] The interfacial phenomenon is due to the accumulation of charges at the grain boundary and as temperature rises, more charges accumulate at the grain boundary thus increases the polarization [8]. According to Sarah and Suryanarayana [49], polarization in ferrites is similar to that of the conduction process. Electrons are locally displaced in the direction of the applied field during the electron exchange between the ferrous (Fe^{2+}) and ferric (Fe^{3+}) ions on the octahedral sites and this determines the polarization [8].

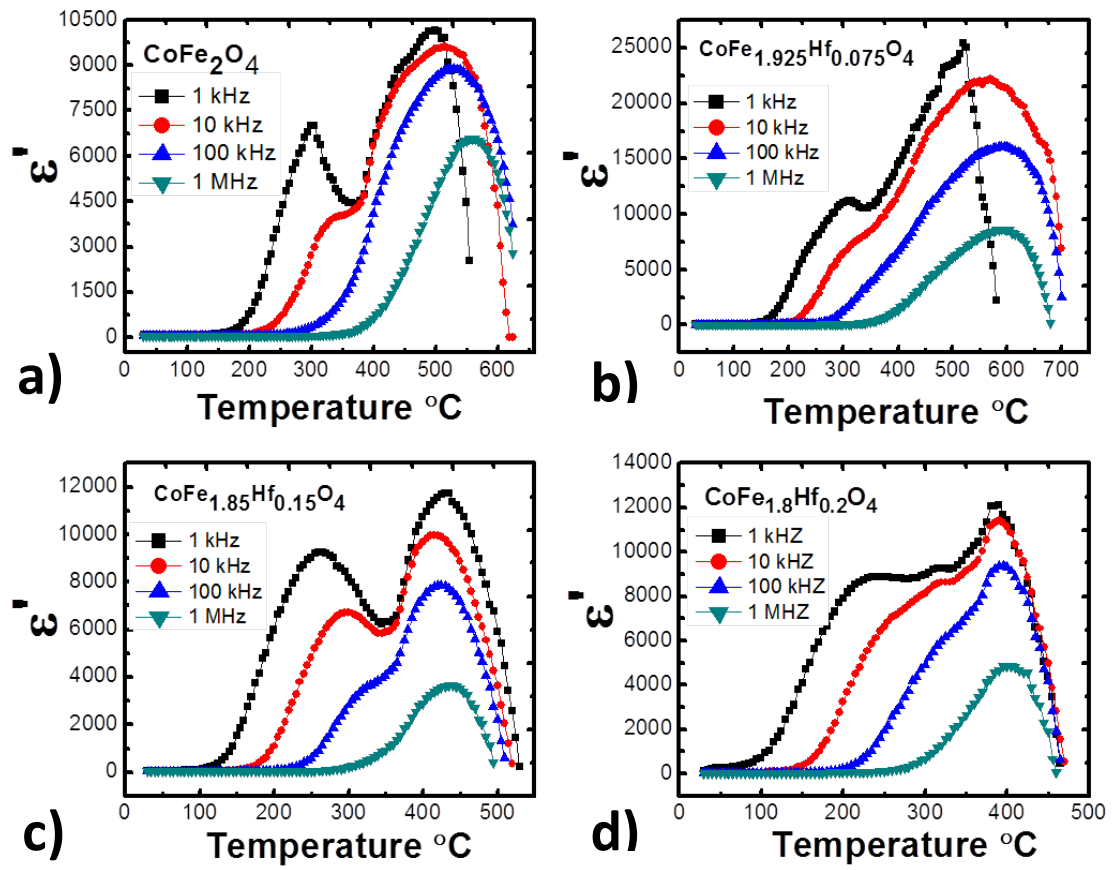


Figure 3.7 Temperature dependent dielectric constant for a given composition

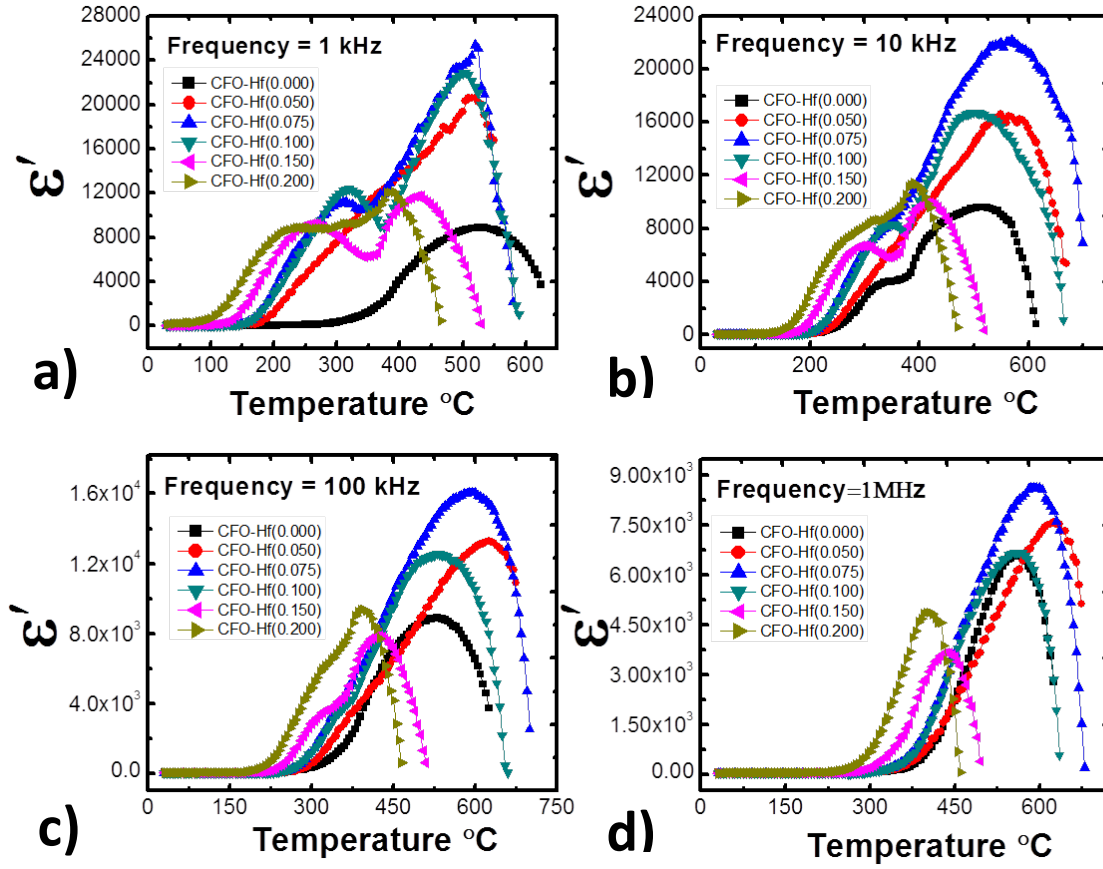


Figure 3.8 Temperature dependent dielectric constant at a constant frequency. The data shown are for various compositions of Hf content in ceramics.

3.7 Temperature Dependent Dielectric Loss Tangent ($\tan \delta$)

The energy loss (dielectric loss tangent, $\tan \delta$) is expressed as the ratio of the imaginary part of the dielectric constant to the real part, (see equation 3). The $\tan \delta$ values depend on impurities, imperfections in the crystal, Fe^{2+} content, and stoichiometry and therefore depend on the composition and sintering temperature of the samples [43]. Both temperature and frequency appear to affect the behavior of the peaks. The data for Hf-integrated cobalt ferrites are shown in Figure 3.9, where a peaking behavior for the energy loss when displayed as a function of temperature is evident for all compositions. The high

energy loss experienced at low frequencies can be explained based on Koop's phenomenological theory [46], in which the resistivity is high and the grain boundaries play a bigger role, more energy is required for the electron transfer between Fe^{2+} and Fe^{3+} ions, as a result the loss is high. At higher frequencies, where the resistivity is low and the grains play the dominant role, less energy is required for the transfer of electrons between the hetero-valent Fe ions and a lower loss is produced. The $\tan \delta (F)$ behavior is said to occur due to a strong correlation between the conduction mechanism and dielectric behaviors that ferrites possess [47]. The maximum of $\tan \delta$ values (Debye relaxation peaks) are expected to occur when the hopping frequency of electrons between Fe^{2+} and Fe^{3+} ions is approximately equal to that of the externally applied field [47]. Since $\omega\tau = 1$, $\omega = 2\pi f$, and $\tau = 1/(2P)$ where P is the jumping probability per unit time then it is expected that f is proportional to P . The shift of peaks to higher temperature with increasing frequency indicates that the jumping probability per unit time ' P ' increases with increasing frequency. However, the shift in peak towards a lower temperature with increasing hafnium ion substitution indicates a decrease in the jumping probability per unit time as hafnium content increases. The decrease in jumping probability is accredited to a reduction of iron ions at the B-site, which is responsible for polarization in these ferrites [47]. As the frequency increases, the peak shifts towards the higher temperature while they shift towards a lower temperature with increasing Hafnium ion substitution as seen in (Fig. 3.9a-d). It is also observed that there is a greater loss tangent or peak height with increasing hafnium concentration and frequency.

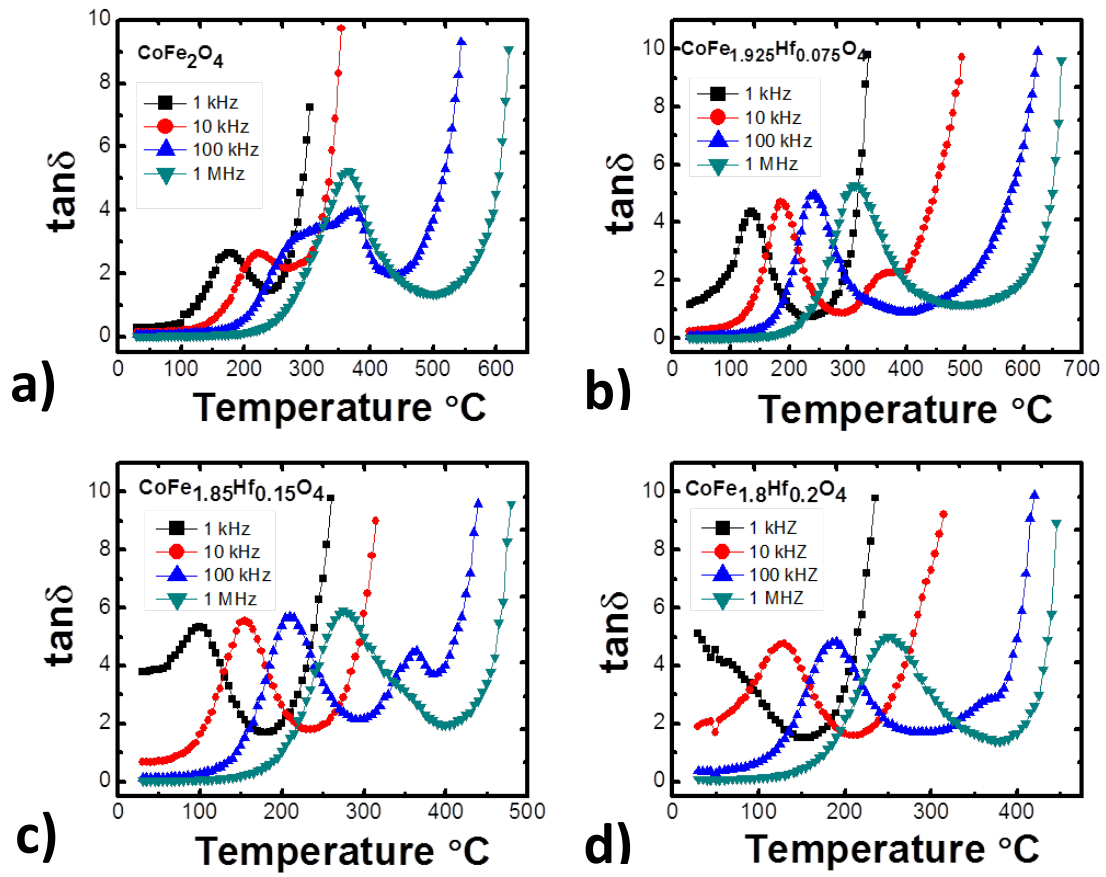


Figure 3.9 Temperature dependent dielectric energy loss for a given composition

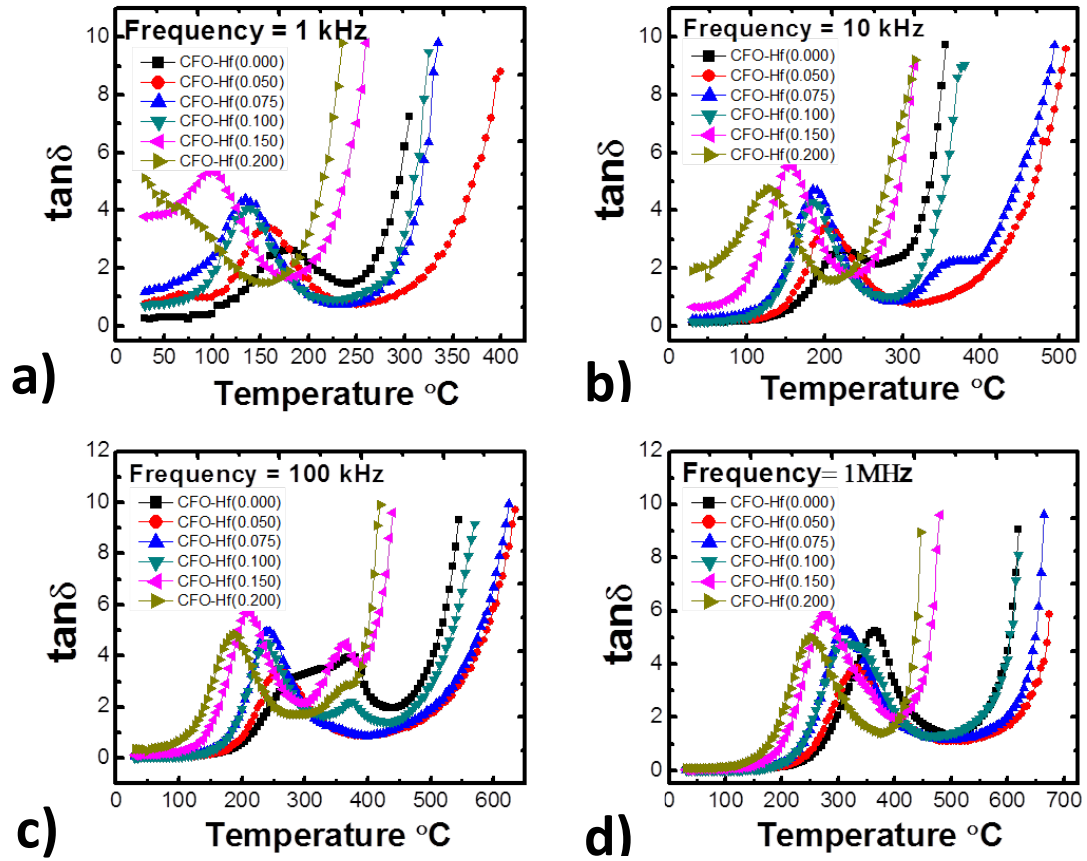


Figure 3.10 Temperature dependent dielectric energy loss for a given frequency

3.8 Temperature dependent imaginary part of dielectric constant

The imaginary part of the dielectric constant (energy dissipation factor) is related to the real part of the dielectric constant and the energy loss tangent by equation 3. Figures 3.11 and 3.12 are supporting the data from the dielectric energy loss graphs. The shift to higher temperatures for the dissipation factor is also explained through the same concept that it is due to the “P” increases with increasing frequency.

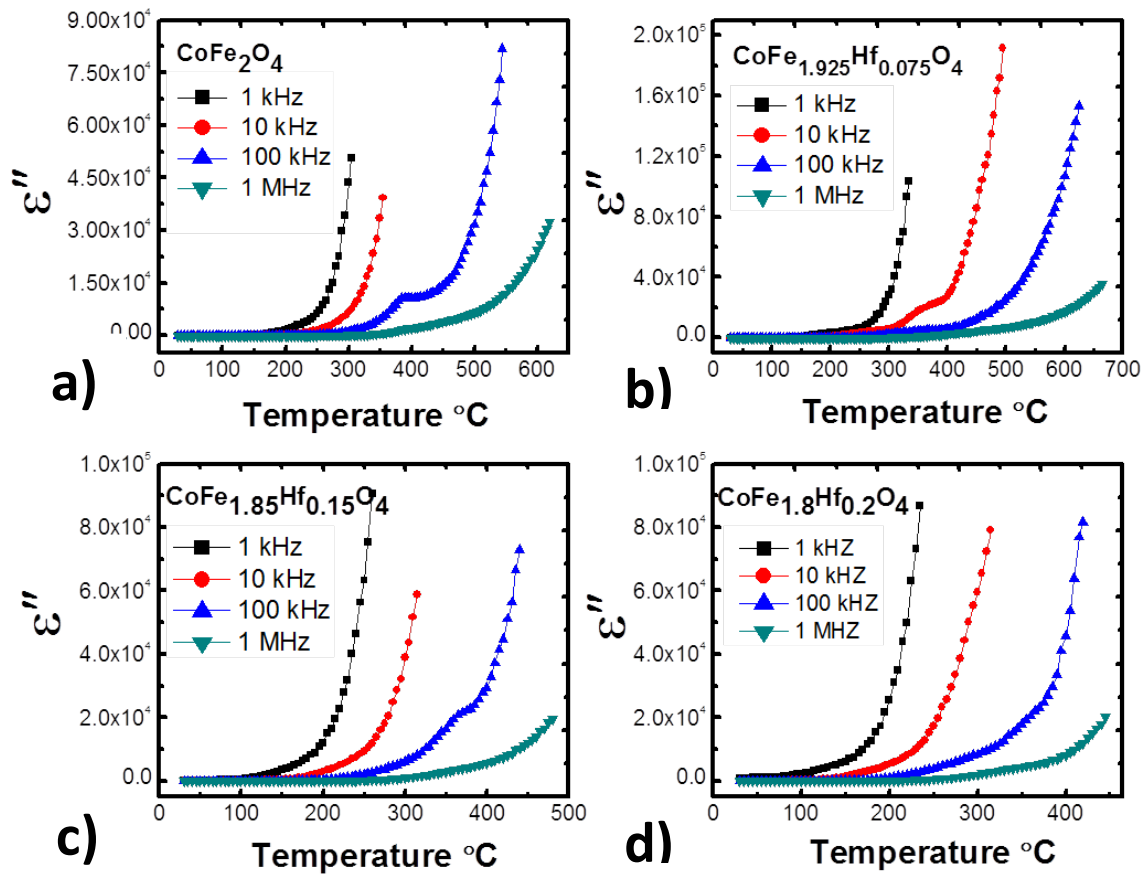


Figure 3.11 Temperature dependent imaginary part of dielectric constant for a given composition

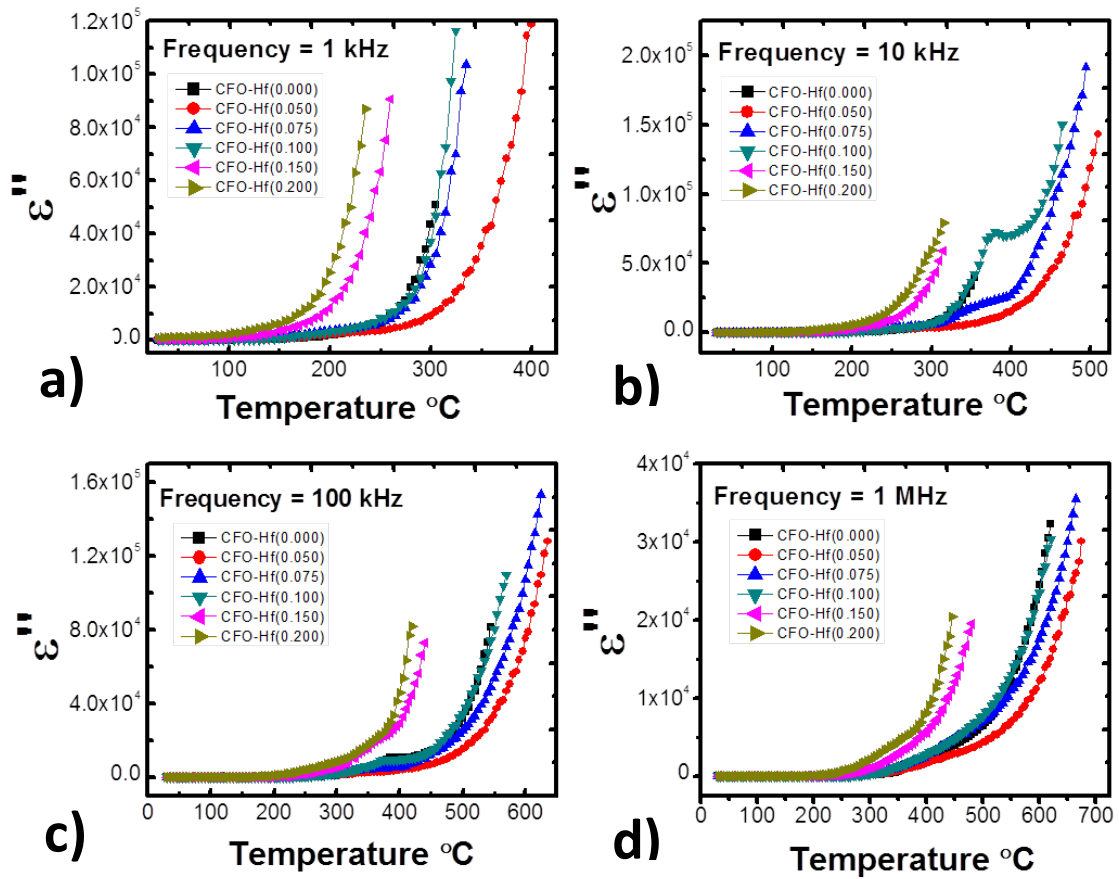


Figure 3.12 Temperature dependent imaginary part of dielectric constant for a given frequency

3.9 Temperature Dependent AC Resistivity

The variation of the ac resistivity with temperature for pure CFO and hafnium integrated cobalt ferrite samples are illustrated in Fig. 3.13. The resistivity initially increases up to 170°C, which increases with increasing frequency, then decreases thereafter. The essential decrease of resistivity implies an increase in the ac conductivity whose increase is more rapid at higher frequencies. This increase in conductivity with temperature is due to the increase in the drift mobility of the charge carriers which leads to increased hopping mechanism. The difference in resistivity values with temperature for the different frequencies indicates the strong frequency dependence under these conditions. As temperature rises, the

resistivity values for all frequencies merge onto a common value. This observed behavior of the conductivity is indicative that electrical conduction in these samples is a thermally activated process governed by the release of space charge in good agreement with the impedance analysis results. Therefore, the peaks observed for all compositions and four frequencies (Fig. 3. 14) may be correlated to the grain and grain boundary contributions implying the space charge contribution to the resistivity becoming dominant above the peak observed in the resistivity. Furthermore, it was interesting to see that the temperature at which the dielectric constant begins to increase, the temperature at which the contribution from the grain boundary initiates in the complex impedance measurements is correspondent to the temperature at which the resistivity peak is observed. All in all, the electrical conduction present with change in compositions at a given frequency may be correlated to the space charge generated due to the thermally activated processes in addition to the hopping of electrons between $\text{Fe}^{2+}/\text{Hf}^{4+}$ and $\text{Fe}^{3+}/\text{Hf}^{4+}$ [Y.D. Kolekar].

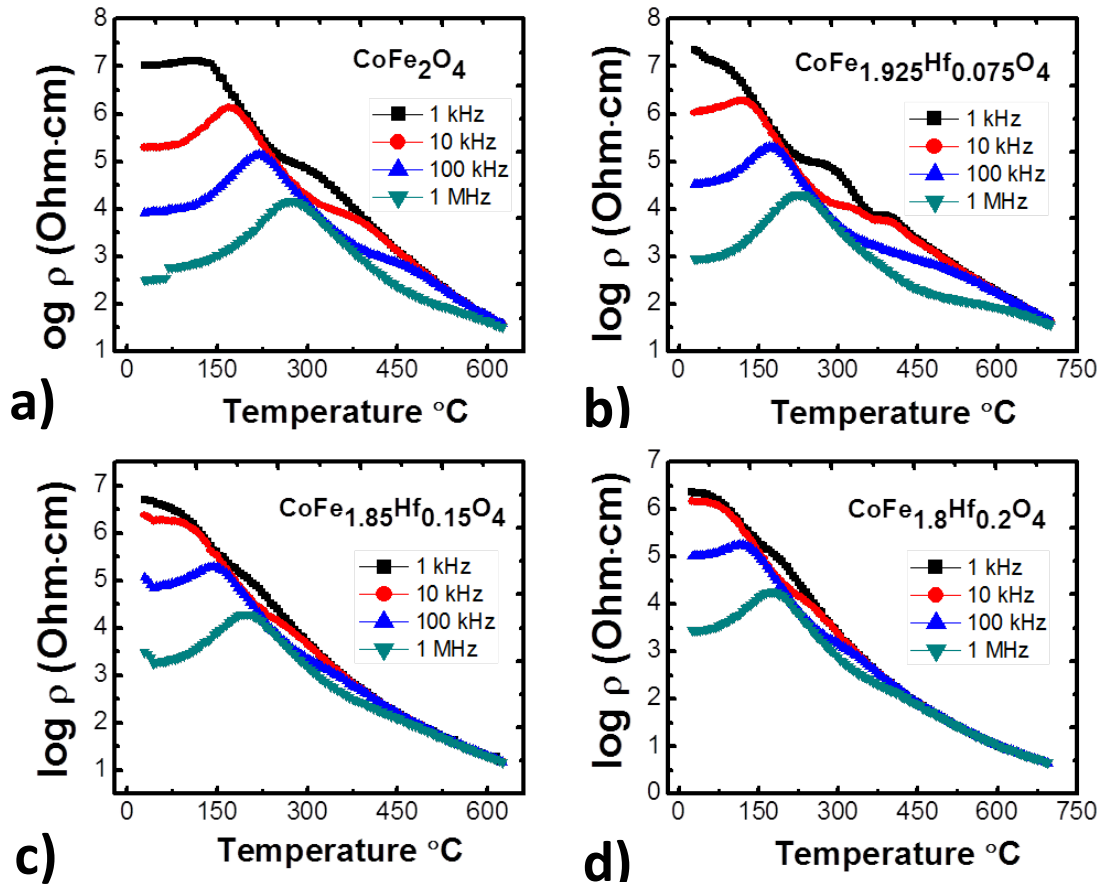


Figure 3.13 Temperature dependent Resistivity for a given composition

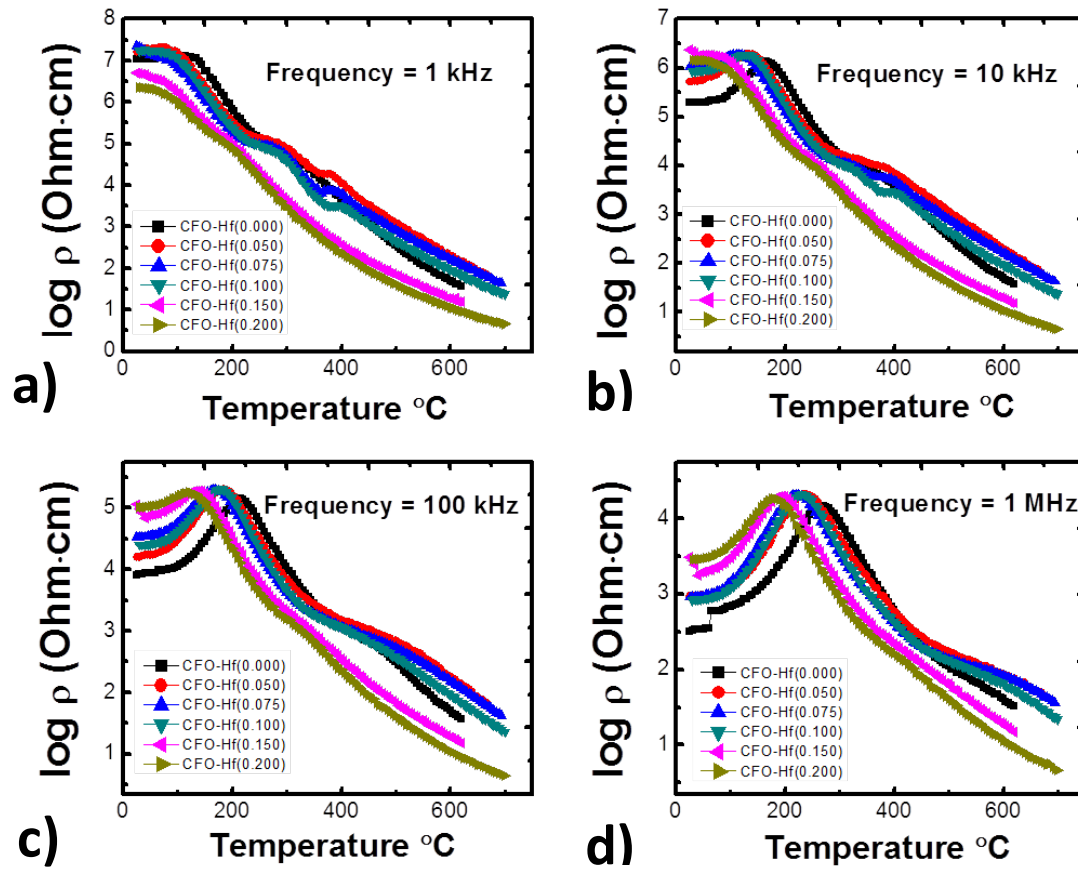


Figure 3.14 Temperature dependent resistivity for a given frequency

3.10 Cole-Cole Plot

A distribution of relaxation times is necessary to interpret the experimental dielectric data and we shall discuss the approach based on a distribution of relaxation times. However, to take into account the effect of a distribution of relaxation times, Cole and Cole have proposed that an Argand diagram, in which Z' (real part of impedance) is plotted as a function of Z'' (imaginary part of impedance) [48].

Debye's semicircle is based on $\alpha = 0$, which represents the materials' having only one single relaxation time. In general, there exists a distribution of relaxation times in all solid materials because there are always some non-uniformities in local domains, which would alter the individual dipoles or charges in addition to the existing dipoles in the material. If the

relaxation times are due to several different mechanisms, then the Z' versus Z'' arc will be asymmetrical [48].

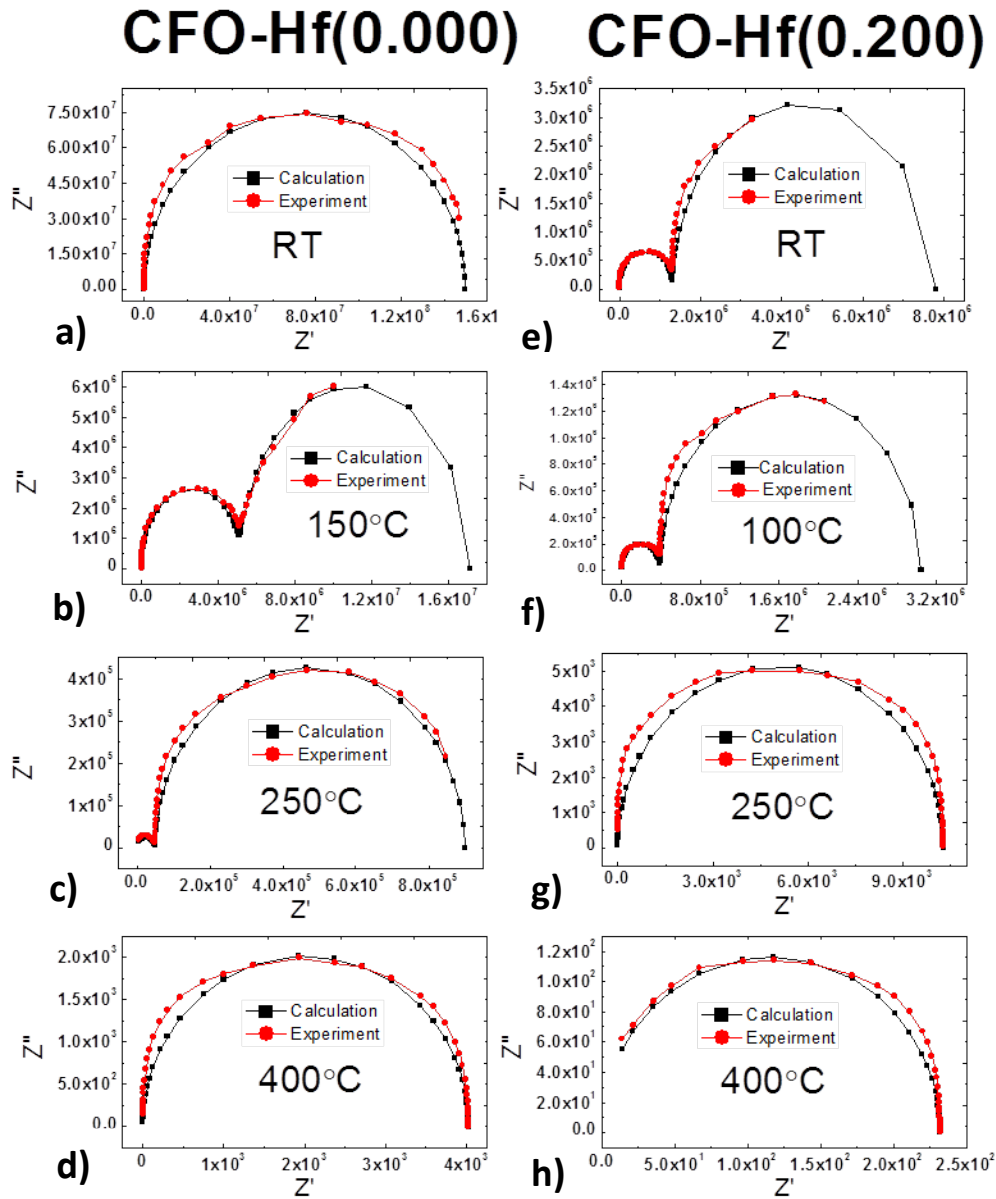


Figure 3.15 Complex impedance spectroscopy for pure CFO and CFO-Hf(0.200) with varying temperature

The following equations were used to obtain the calculated complex impedance spectroscopy data:

$$Z^* = \frac{1}{R_g^{-1} + j\omega C_g} + \frac{1}{R_{gb}^{-1} + j\omega C_{gb}} = Z' - jZ''$$

$$Z' = \frac{R_g}{1 + (\omega R_g C_g)^2} + \frac{R_{gb}}{1 + (\omega R_{gb} C_{gb})^2}$$

$$Z'' = \frac{\omega R_g^2 C_g}{1 + (\omega R_g C_g)^2} + \frac{\omega R_{gb}^2 C_{gb}}{1 + (\omega R_{gb} C_{gb})^2}$$

Where Z^* is the complex impedance, Z' is the real part of the impedance, Z'' is the imaginary part of the impedance, R_g , R_{gb} and C_g , C_{gb} are the resistance and capacitance of the respective grain and grain boundaries.

3.11 Complex Impedance Plots - Grain and Grain Boundary Contribution

The impedance plots for pure CFO and CFO-Hf(0.200) obtained at different temperatures (30-400°C) are shown in (Fig. 3.15). The effect of Hf is clearly evident on the electrical behavior at all temperatures when both compositions are compared. At room temperature (30°C), a single semicircular arc is observed for pure CFO. The corresponding plot for CFO-Hf at 30°C has a different behavior. This one shows two semicircular arcs. This observation indicates that the dielectric response and associated mechanism is different in CFO-Hf when compared to pure CFO. The reader should be informed that the diameter of the semicircles represents the resistance from the respective grain and/or grain boundary. Further analysis of the impedance data as a function of T for CFO and CFO-Hf provides additional insight into the detailed mechanisms. The decreasing diameter behavior of the left semicircle resulting from grain for both compositions, pure and CFO-Hf(0.2) indicates that the conductivity from the bulk increases with increasing temperature. For pure CFO, there is no grain boundary contribution to permittivity at room temperature until higher temperatures. While for CFO-Hf(0.200), the grain boundary plays a dominant role from room temperature throughout which leads to higher polarization effects.

The resistance and capacitance behavior according to grain and grain boundary contribution is indicated in Table 2.

Table 2 Grain (g) and grain boundary (gb) electric response to Hf content

Temp. (K)	CoFe ₂ O ₄				CoFe _{1.9} Hf _{0.1} O ₄				CoFe _{1.8} Hf _{0.2} O ₄			
	R _g (MΩ)	C _g (pF)	R _{gb} (MΩ)	C _{gb} (pF)	R _g (MΩ)	C _g (pF)	R _{gb} (MΩ)	C _{gb} (pF)	R _g (MΩ)	C _g (pF)	R _{gb} (MΩ)	C _{gb} (pF)
300	150	7	--	--	16.5	8	21	500	1.31	7	6.5	1850
323	88	12	--	--	14.5	8	21	550	0.78	9	5	2200
373	28	10	--	--	5.5	8	16	900	0.393	9	2.65	2300
423	5.15	9	12.000	800	0.525	8	9.5	1550	0.071	9	0.512	2300
473	0.54	9	5.820	1500	0.052	8	1.42	2500	0.01	9	0.065	2300
523	0.05	8	0.850	2400	0.004	8	0.0695	3000	--	--	0.01	2300
573	0.006	8	0.011	2600	0.001	8	0.0145	3025	--	--	0.001	2300
623	--	--	0.016	2700	--	--	0.0026	3025	--	--	5E-4	2300
673	--	--	0.004	2750	--	--	0.0016	3050	--	--	2E-4	2700

The parameters in table 2 were obtained by fitting the data from the complex impedance spectroscopy.

The effect of Hf and the physics behind the observed transition from grain dominated mechanism (CFO) to grain boundary dominated effects on the dielectric properties of CFO-Hf can be understood as follows. Hafnium is larger in size and, so, its incorporation into CFO expands the lattice. The increase in ϵ' with Hf is, thus, due to the atomic polarizability resulting from CFO-Hf composite formation. The distance between the cations in the CFO-Hf are larger compared to pure CFO. This mechanism accounts for the observed $\epsilon'(T)$ dependence on composition (x) of CFO-Hf. In addition, Hf ions form the secondary phase at the grain boundary. The secondary phase formed at the grain boundary is more insulating compared to the interior of the grain. The charge accumulation at grain boundaries contribute to the interfacial polarization, which further enhances the dielectric constant as noted for CFO-Hf. Some of the Hf ions substituting for Fe may result in Fe^{2+} ions (for charge

neutrality), which makes grains more conducting compared to grain boundaries. Furthermore, the charge concentration gradient with a separation barrier at grain boundary to grain interface occurs due to Hf^{4+} ions at the boundary versus $\text{Fe}^{3+}/\text{Fe}^{2+}$ ions within the bulk of the grain. Evidence for such mechanism is derived from impedance spectroscopic data, where initially CFO exhibits one semicircular arc (grain) while CFO-Hf exhibits two semicircular arcs (grain and grain boundary). However, increasing temperature increases the electron hopping within the grain, making it more conducting, and finally the grain-effect diminishes, at which point the grain-boundary effect alone contributes to the dielectric relaxation. A direct, microscopic evidence for HfO_2 phase at the grain boundaries is provided by the scanning electron microscopy (SEM) imaging coupled with energy dispersive X-ray spectrometry (EDS) analysis as shown in Fig. 3.16 for $x=0.075$. The image A shown is on a larger scale bar to indicate the CFO grains. The magnified phase contrast image (B; inset) shows the expanded region of the grain boundary, where the white HfO_2 insulating particles are evident all along the edges of the CFO grains. Thus, impedance and microscopy analyses clearly confirm and validate the proposed model of semiconducting-grains (CFO) separated by insulating-grain boundaries (HfO_2).

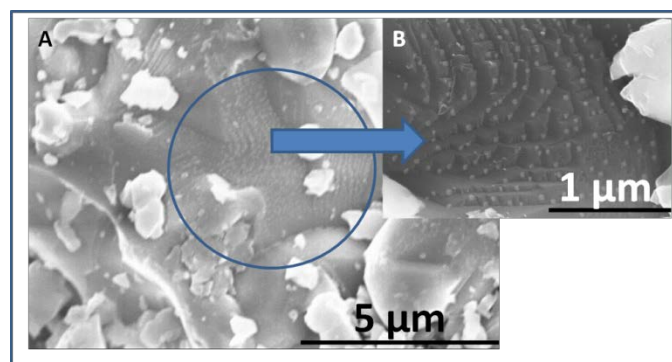


Figure 3.16 SEM data for $x=0.075$. The image A shown is on a larger scale bar to indicate the CFO grains. The magnified phase contrast image (B; inset) shows the expanded region of the grain boundary, where the white HfO_2 insulating particles are evident all along the edges of the CFO grains.

Chapter 4: Conclusions

Hafnium integrated cobalt ferrite was fabricated using the solid state reaction method. The results show that the temperature and frequency of the externally applied field had a significant effect on the dielectric constant, loss, and conductivity properties. The SEM image for CFO-Hf(0.200) appear to show hafnium particles residing at the grain boundaries. At room temperature, the dielectric constant is higher in the low frequency range, especially when the hafnium concentration is higher. The loss energy is maximum for the Hf(0.1) sample at room temperature and at Hf(0.15) with temperature. Conductivity increases as Hf content increases. When the dielectric constant was plotted as function of temperature, the highest value achieved was 25,384 at Hf(0.075) at 520°C with frequency of 1kHz. This high value is attributed to the presence of Hf at the grain boundaries when ($\text{Hf} > 0.075$). The integration of hafnium in cobalt ferrite, in concentration (>0.075), increased the amount of Fe^{2+} which in turn increased the conductivity due to increased electron exchanges between Fe^{2+} and Fe^{3+} . Finally, the grain boundary plays a major role with $\text{Hf} > 0.075$ which leads to higher dielectric constant values. At room temperature, Hf-induces a transition from grain-dominated mechanism to grain-boundary dominated mechanism of the dielectric relaxation in CFO. The dielectric maxima occur at lower temperatures in CFO-Hf compared to CFO due to formation of insulating grain boundaries with increasing Hf-content. The results demonstrate that the dielectric properties of CFO-Hf can be tailored by tuning the Hf concentration.

References

1. Cullity B.D., C.D. Graham. Introduction to Magnetic Materials. Hoboken: John Wiley & Sons, Inc. 2009. Book.
2. K. Khaja Mohaideen, P.A.Joy Influence of initial particle size on the magnetostriction of sintered cobalt ferrite derived from nanocrystalline powders. Journal of Magnetism and Magnetic Materials 346(2013)96–102.
3. R.W. McCallum, K.W. Dennis, D.C. Jiles, J.E. Snyder, Y.H. Chen Composite magnetostrictive materials for advanced automotive magnetomechanical sensors Low Temperature Physics, 27 (2001), pp. 266–274
4. Ovidiu Caltuna, G.S.N. Rao, K.H. Rao, B. Parvatheeswara Rao, Ioan Dumitru, Chong-Oh Kim, CheolGi Kim The influence of Mn doping level on magnetostriction coefficient of cobalt ferrite. Journal of Magnetism and Magnetic Materials 316 (2007) 618–620
5. K. P. Belov and M. A. Zaitseva. New magnetic materials-garnet ferrites. Soviet Physics Uspekhi vol. 66-1. 1958.
6. Pullar, Robert C. Magnetic hexaferrites have an attractive future. Ceramics.org. The American Ceramic Society (2012). Web. 18 July 2013.
7. Yuri S. Didosyan et al. Sensors and Actuators in Orthoferrites. IEEE (2004). Web. 20 July 2013.
8. Abdul Samee Fawzi, A.D. Sheikh, V.L. Mathe. Structural, dielectric properties and AC conductivity of $\text{Ni}(1-x)\text{Zn}_x\text{Fe}_2\text{O}_4$ spinel ferrites. Alloys and Compounds. 502 (2010) 231–237.
9. T. Abraham J. Am. Ceramic. Soc. Bull., 73 (1994), p. 62

10. A.M.Bhavikatti, DR.Subhash Kulkarni, DR. Arunkumar. Lagashetty “Evaluation of AC conductivity & dielectric behavior of cobalt ferrite” A.M.Bhavikatti et al. / International Journal of Engineering Science and Technology (IJEST).
11. S. Wells, C.V. Ramana, Effect of hafnium-incorporation on the microstructure and dielectric properties of cobalt ferrite ceramics, *Ceramics International* (2013), <http://dx.doi.org/10.1016/j.ceramint.2013.05.073>.
12. A. Rafferty, T. Prescott, D. Brabazon Sintering behavior of cobalt ferrite ceramic *Ceramics International*, 34 (2008), pp. 15–21
13. H. Yünger, E. Ozel Effect of milling process on the properties of CoFe_2O_4 *Ceramics International*, 39 (2013), pp. 5503–5511
14. K. Kamala Bharathi, G. Markendeyulu, C.V. Ramana Structural, magnetic, electrical, and magnetoelectric properties of Sm- and Ho-substituted nickel ferrites *Journal of Physical Chemistry C*, 115 (2011), pp. 554–560
15. K. Kamala Bharathi, G. Markendeyulu, C.V. Ramana Enhanced dielectric property of Ni ferrite by Sm and Ho substitution *Electrochemical and Solid-State Letters*, 13 (2010), pp. G98–G102
16. Z. Gu, X. Xiang, G. Fan, F. Li Facile synthesis and characterization of cobalt ferrite nanocrystal via a simple reduction–oxidation route *Journal of Physical Chemistry C*, 112 (2008), pp. 18459–18466
17. U. Kurtan, R. Topkaya, A. Baykal, M.S. Toprak Temperature dependent magnetic properties of CoFe_2O_4 /CTAB nanocomposite synthesized by sol–gel auto-combustion method *Ceramics International*, 39 (2013), pp. 6551–6558
18. R. Peelamedu, C. Grimes, D. Agrawal, R. Roy, P. Yadoji Ultralow dielectric constant nickel–zinc ferrites using microwave sintering

19. W. Eerenstein, N.D. Mathur, J.F. Scott Multiferroic and magnetoelectric materials *Nature*, 442 (2006), pp. 759–765
20. M. Fiebig Revival of magnetoelectric effect *Journal of Physics D: Applied Physics*, 38 (2005), pp. R123–R152
21. E. Manova, B. Kunev, D. Paneva, I. Mitov, L. Petrov Mechano-synthesis, characterization, and magnetic properties of nanoparticles of cobalt ferrite, CoFe_2O_4 *Chemistry of Materials*, 16 (2005), pp. 5689–5696
22. Q. Song, Z.J. Zhang. Correlation between spin–orbital coupling and the superparamagnetic properties in magnetite and cobalt ferrite spinel nanocrystals *Journal of Physical Chemistry B*, 110 (2006), pp. 11205–11209
23. Y.N. Nuli, Q.Z. Qiu Nanocrystalline transition metal ferrite thin films prepared by an electrochemical route for Li-ion batteries *Journal of Power Sources*, 142 (2005), pp. 292–297
24. G.L. Sun, J.B. Li, J.J. Sun, X.Z. Yang The influences of Zn^{2+} and some rare-earth ions on the magnetic properties of nickel–zinc ferrites *Journal of Magnetism and Magnetic Materials*, 281 (2004), pp. 173–177
25. N. Rezlescu, E. Rezlescu, C. Pasnicu, M.L. Craus Effects of the rare-earth ions on some properties of nickel–zinc ferrite *Journal of Physics: Condensed Matter*, 6 (1994), pp. 5707–5716
26. M. Ajmal, A. Maqsood Influence of zinc substitution on structural and electrical properties of $\text{Ni}_{1-x}\text{Zn}_x\text{Fe}_2\text{O}_4$ ferrites *Materials Science and Engineering B*, 139 (2007), pp. 164–170
27. S. Amiri, H. Shokrollahi The role of cobalt ferrite magnetic nanoparticles in medicine *Materials Science and Engineering C*, 33 (2013), pp. 1–8

28. Mohd. Hashim, Alimuddin, Shalendra Kumar, Sagar E. Shirsath, R.K. Kotnala, Jyoti Shah d, Ravi Kumar “ Synthesis and characterizations of Ni^{+2} substituted cobalt ferrite Nanoparticles “Materials Chemistry and Physics 139 (2013) 364-374
29. M.A. Gabal a,!, Y.M. Al Angari a, F.A. Al-Agel Synthesis, characterization and magnetic properties of Cr-substituted Co–Zn ferrite nanopowders. Journal of Molecular Structure 1035 (2013) 341–347. .
30. D. Ravinder), A.V. Ramana Reddy, G. Ranga Mohan Abnormal dielectric behaviour in polycrystalline zinc-substituted manganese ferrites at high frequencies. Materials Letters 52 Ž2002. 259–265.
31. Yuksel Koseoglu Structural, magnetic, electrical and dielectric properties of $MnxNi1-xFe2O4$ spinel nanoferrites prepared by PEG assisted hydrothermal method. Ceramics International 39 (2013) 4221–4230.
32. Yuksel Koseoglu, Furkan Alan, Muhammed Tan, Resul Yilgin, Mustafa Ozturk. Low temperature hydrothermal synthesis and characterization of Mn doped cobalt ferrite nanoparticles. Ceramics International 38 (2012) 3625–3634.
33. H. Arobi, F. Ganjali. Structural and Magnetic Properties of Cobalt and Manganese Doped Ni-Ferrite Nanoparticles. J Supercond Nov Magn (2013) 26:1031–1035.
34. Mahmoud Goodarz Naseri, Elias B. Saion, Hossein Abbastabar Ahangar, Abdul Halim Shaari, and Mansor Hashim, Simple Synthesis and Characterization of Cobalt Ferrite Nanoparticles by a Thermal Treatment Method. Journal of Nanomaterials Volume (2010).
35. S.R. Ahmed, S.B. Ogale, G.C. Papaefthymiou, R. Ramesh, P. Kofinas Magnetic properties of $CoFe_2O_4$ nanoparticles synthesized through a block copolymer nanoreactor route Appl. Phys. Lett., 80 (2002), pp. 1616–1618
36. I. Brigger, C. Dubernet, P. Couvreur Nanoparticles in cancer therapy and diagnosis Adv. Drug Delivery Rev., 54 (2002), pp. 631–651

37. R. Arulmurugan, G. Vaidyanathan, S. Senthilnathan, B. Jeyadevan Mn-Zn ferrite nanoparticles for ferrofluid preparation: study on thermal-magnetic properties J. Magn. Magn Mater., 298 (2006), pp. 83–94
38. J.B. Haun, T.J. Yoon, H. Lee, R. Weissleder Magnetic nanoparticle biosensors Wiley Interdiscip. Rev. Nanomed. Nanobiotechnol., 2 (2010), pp. 291–304
39. L. Jianjun, Y. Hongming, L. Guodong, L. Yanju, L. Jinsong Cation distribution dependence of magnetic properties of sol–gel prepared MnFe_2O_4 spinel ferrite nanoparticles J. Magn. Magn Mater., 322 (2010), pp. 3396–3400
40. J. Amighian, M. Mozaffari, B. Nasr Preparation of nano-sized manganese ferrite (MnFe_2O_4) via coprecipitation method Phys. Status Solidi C, 3 (2006), pp. 3188–3192
41. C. Liu, B. Zhou, A. J. Rondinone, Z. J. Zhang Reverse Micelle Synthesis and Characterization of Superparamagnetic MnFe_2O_4 Spinel Ferrite Nanocrystallites J. Phys. Chem. B, 104 (2000), pp. 1141–1145
42. D. Zhang, X. Zhang, X. Ni, J.M. Song, H. Zheng Low-temperature fabrication of MnFe_2O_4 octahedrons: magnetic and electrochemical properties Chem. Phys. Lett., 426 (2006), pp. 120–123
43. Muhammad Ajmal, A. Sghari Maqsood. Influence of zinc substitution on structural and electrical properties of $\text{Ni}_{1-x}\text{Zn}_x\text{Fe}_2\text{O}_4$ ferrites. Materials Science and Engineering B 139 (2007) 164–170.
44. B. Aguirrea, R.S. Vemuria, D. Zubiaa, M.H. Engelhardb, V. Shutthanadanb, K. Kamala Bharathic, C.V. Ramana, Growth, microstructure and electrical properties of sputter-deposited hafnium oxide (HfO_2) thin films grown using a HfO_2 ceramic target. Applied Surface Science 257 (2011) 2197–2202.

45. T.M. Meaza, S .M. Attiab, A .M. Abou El Ata Effect of tetravalent titanium ions substitution on the dielectric properties of Co–Zn ferrites. *Journal of Magnetism and Magnetic Materials* 257 (2003) 296–305.
46. Zorica Z. Lazarevic' Cedomir Jovalekic Dalibor L .Sekulic Aleksandra Milutinovic Sebastian Balos Milos Sankamenac Nebojsa Z. Romcevi. Structural, electrical and dielectric properties of spinel nickel ferrite prepared by soft mechanochemical synthesis. *Materials Research Bulletin* (2013).
47. Schönhalz and F. Kremer. Analysis of Dielectric Spectra. *Broadband Dielectric Spectroscopy*. Berlin: Springer, 2003. 59-96.
48. Kao, Kwan Chi. *Dielectric Phenomena In Solids*. San Diego: Elsevier, 2004. Book.
49. P. Sarah, S.V. Suryanarayana, *Indian J. Phys.* 77 (2003) 449.
50. Kalendová, D. Veselý, J. Brodinová, (2004) "Anticorrosive spinel-type pigments of the mixed metal oxides compared to metal polyphosphates", *Anti-Corrosion Methods and Materials*, Vol. 51 Iss: 1, pp.6 – 17.
51. "Crystal Structure." www.geocities.jp. n.p., n.d. Web. 12 July 2013.
52. Daniel Jurgens. X-ray Diffraction. *Atomic and Nuclear Physics*. Institute of Physics. 11 July 2013. Web. 18 July 2013.

Curriculum Vita

Luis J. Sanchez was born in Ciudad Juarez, Chihuahua. The first son of Victor Javier Sanchez Pena and Isabel Flores. He graduated from Franklin High School, El Paso, TX in the spring of 2006 and entered the University of Texas at El Paso in the Fall of 2007. While pursuing a bachelor's degree in metallurgical engineering, he participated in the concrete canoe division of the American Society of Civil Engineers for three years. After graduating in May 2012 he spent the summer interning at Vallourec and Mannesman Tubes in Houston TX. In the fall of 2012, he entered the Graduate School at the University of Texas at El Paso.

Permanent Address: 7391 Lakehurst
 El Paso TX, 79912